Patterns and coherence resonance in the stochastic Swift-Hohenberg equation with Pyragas control: the Turing bifurcation case

Kuske, R.; Lee, C.Y.; Rottschäfer, V.

Physica D 365 (2018) 57–71

Contents lists available at ScienceDirect

Physica D

journal homepage: www.elsevier.com/locate/physd

Patterns and coherence resonance in the stochastic Swift–Hohenberg equation with Pyragas control: The Turing bifurcation case

R. Kuske [a], C.Y. Lee [a,1], V. Rottschäfer [b,*]

[a] Department of Mathematics, University of British Columbia, 1984 Mathematics Road, Vancouver, BC, Canada V6T 1Z2
[b] Mathematical Institute, Leiden University, P.O. Box 9512, 2300 RA Leiden, The Netherlands

HIGHLIGHTS

- Both Turing or Turing–Hopf bifurcations possible through feedback and length of delay.
- Delays drive dynamics on new time scale, intermediate to usual slow and fast scale.
- Interaction of delay and noise influences existence and stability result of patterns.
- Approximate spectral densities show oscillations sustained via coherence resonance.

ARTICLE INFO

Article history:
Received 31 August 2016
Received in revised form 18 October 2017
Accepted 24 October 2017
Available online 23 November 2017
Communicated by T. Wanner

Keywords:
Swift–Hohenberg equation
Stochastic pattern dynamics
Pyragas control
Delayed feedback
Coherence resonance
Multiple time scales analysis

ABSTRACT

We provide a multiple time scales analysis for the Swift–Hohenberg equation with delayed feedback via Pyragas control, with and without additive noise. An analysis of the pattern formation near onset indicates both the possibility of either standing waves (rolls) or traveling waves via Turing or Turing–Hopf bifurcations, respectively, depending on the product of the strength of the feedback and the length of the delay. The remainder of the paper is focused on Turing bifurcations, where the delay can drive the appearance of an additional time scale, intermediate to the usual slow and fast time scales observed in the modulation of rolls without delay. In the deterministic case, a Ginzburg–Landau-type modulation equation is derived that inherits Pyragas control terms from the original equation. The Eckhaus stability criteria is obtained for the rolls, with the intermediate time scale observed in the transients. In the stochastic context, slow modulation equations are derived for the amplitudes of the primary modes that are coupled to a fast Ornstein–Uhlenbeck-type equation with delay for the zero mode driven by the additive noise. By deriving an averaging approximation for the amplitude of the primary mode, we show how the interaction of noise and delay influences the existence and stability range for the noisy roll-type patterns. Furthermore, approximations for the spectral densities of the primary and zero modes show that oscillations on the intermediate times scale are sustained through the phenomenon of coherence resonance. These dynamics on the intermediate time scale are sustained through the interaction of noise and delay, in contrast to the deterministic context where dynamics on the intermediate times scale are transient.

1. Introduction

Understanding the spontaneous emergence of patterns in spatially extended systems which are not in equilibrium has been a topic of interest for many years. These studies are motivated by examples in fluid dynamics, nonlinear optics, chemical reactions, and mathematical biology to just name a few. General surveys are given by, for example, Cross and Hohenberg [1], Cross and Greenside [2], Hoyle [3], and Pismen [4]. In many cases the patterns that appear are roughly periodic in space with an amplitude that grows as a control parameter is increased above a critical value. However, these patterns are often unstable leading to a variety of possible states, including hybrid states of bistable patterns and spatio-temporal chaos. One of the challenges is to develop control schemes that stabilize either simple steady states or simple patterned states, so that a desired, otherwise unstable, solution may be realized. Certain types of control schemes include time delayed feedback that may contribute to the stability, as discussed in [5] and [6] and references therein, covering applications in chemistry, biology, optics, and ecology. Likewise, understanding the effects

* Corresponding author.
E-mail address: vivi@math.leidenuniv.nl (V. Rottschäfer).
[1] Present address: AIR Worldwide, Boston, United States.

https://doi.org/10.1016/j.physd.2017.10.012
0167-2789/

of noise on spatially extended systems has long been of interest [7], arising in the contexts of different pattern types, influence of parameter regimes, underlying scaling laws, and control and optimization.

In this article, we study the influence of the **interaction** of noise and time delay on the existence and stability of spatially periodic solutions. The interest in the influence of noise and delay in spatial–temporal dynamics has led to theoretical results on qualitative properties like existence, uniqueness, and stability of stochastic partial differential equations with delays, as well as on networks of stochastic ordinary differential equations with delay, too numerous to recount here. Capturing quantitative behavior of spatial patterns in stochastic partial differential equations with delay has been primarily confined to numerical studies as in [8,9] or to small delay approximations [10,11] that are typically valuable only for analyzing steady state equilibria. In contrast, there have been few quantitative analytical results on spatial patterns which capture the combined influence of noise and delayed feedback.

A canonical model equation for the analysis of the dynamics of pattern forming systems is the Swift–Hohenberg equation (SHE). Originally derived in the context of convective instability in the Rayleigh–Bénard model [12], the SHE has been studied as a simplified model to understand the key pattern forming mechanisms and to provide insight into pattern formation in more complicated systems. In order to study the effect of delay and noise on pattern formation, we consider the SHE with Pyragas control and additive white noise: the stochastic Swift–Hohenberg equation with Pyragas control (SHE+P),

$$du = \left[-(1+\partial_x^2)^2 u + ru - u^3 + a(u - u(t-\tau))\right] dt + \tilde{\sigma}\, dB(t). \tag{1.1}$$

Here r is the parameter that usually plays the role of the bifurcation parameter in the SHE and the standard Brownian motion $B(t)$ has noise strength $\tilde{\sigma}$. The positive real parameters a and τ characterize the time-delayed feedback $a(u(t)-u(t-\tau))$ known as Pyragas control. This form was originally proposed by Pyragas in [13] to extend the parameter range of stability of regular behavior in certain types of dynamical systems with unstable periodic orbits. An important feature of Pyragas control in the SHE is that it maintains the same steady state, in this case the basic state of $u = 0$, thus avoiding the introduction of steady states not observed in the system without control. For $\tau \sim \mathcal{O}(1)$, its key effects are dictated by the product $a\tau$, as commonly observed in other studies, for example [14].

The new aspects of this paper arise in the analytical study of the influence of time-delayed feedback on the formation and stability of spatially periodic patterns (rolls) in the SHE+P, with and without stochastic forcing. In the deterministic case we derive a Ginzburg–Landau-type equation that captures similarities and differences in the evolution of the pattern envelope as compared with SHE. Furthermore we study **analytically** how certain types of pattern dynamics are enhanced by the **interaction** of stochastic forcing and time-delayed feedback—not just one or the other as in the literature discussed below.

Literature

The standard SHE and variants of it have been studied extensively, including with general nonlinearities, temporal or spatial periodic forcing, and in higher dimensions. Beyond the extended spatially periodic patterns that are the focus of this paper, a myriad of other patterns are possible that are not studied here: pattern selection on bounded domains [15], multi-bump patterns [16], and localized patterns related to homoclinic and heteroclinic connections for different types of states [17–21].

Time-delayed feedback in pattern forming systems without noise has been considered in several different contexts. In [6] the FitzHugh–Nagumo model, a simplified model of excitations of membrane potentials, is analyzed in two dimensions in the vicinity of a critical point where the dynamics can be described by the SHE with delay. As demonstrated numerically, the delayed feedback induces a spontaneous motion of localized spots. In the study of nonlinear optical cavities with delayed feedback introduced by an external reflective cavity, the SHE with time-delay is analyzed directly but can also be derived, see for example [22–24]. In general, the delay can lead to (de-)stabilization, oscillatory behavior, or resonance. For the complex Ginzburg–Landau equation with Pyragas control, additional spatial feedback terms are needed to stabilize waves, as shown in one dimension in [25] and in two dimensions in [26]. For the SHE+P, the authors of [27] used a linear analysis and modal decomposition to derive a system of ordinary delay differential equations (DDEs) for certain order parameters characterizing stationary or traveling wave patterns. They investigated the influence of time-delay on the stability properties of a single localized structure, demonstrating numerically that the variation of the product $a\tau$ can lead to the formation of oscillons, soliton rings, or labyrinth patterns. Delay-induced spontaneous motion of localized structures was illustrated numerically in [6,22], while in [5] a linear stability analysis of DDEs for the amplitudes of certain modes was combined with numerical simulations to capture dynamical properties of traveling spatio-temporal patterns in a SHE+P for $a\tau > 1$. They find that variation in the delay time and the feedback strength can lead to complex patterns, including the formation of traveling hexagons, traveling zigzag patterns, or intricate oscillatory structures.

The stochastic SHE without delay ($a = 0$ or $\tau = 0$ in (1.1)) has been studied by [28–33] for periodic and unbounded domains, considering additive or multiplicative noise. With time-dependent additive noise on a periodic domain $[-\pi, \pi]$, formal averaging arguments and rigorous convergence estimates in [31,32] show that under a suitable noise strength, solutions are well-approximated by a dominant pattern with wave number $k_c = 1$ and amplitudes described by Landau-type equations that are coupled to a fast Ornstein–Uhlenbeck process. These results are extended to derive stochastic Landau-type equations in the case of multiplicative noise [28,30], coupled Ginzburg–Landau-type equations in the case of unbounded domains and additive noise [33], and stochastic Ginzburg–Landau equations in the case of space–time white noise on arbitrarily large domains scaling with $\mathcal{O}(\varepsilon^{-1})$ [29]. Other statistical properties of the solution, such as the correlation and power spectra of trajectories of the amplitude, were studied numerically in [34,35]. A modal decomposition and multiple scale analysis is applied to derive coupled amplitude equations for slow and fast modes in the case of the Kuramoto–Sivashinsky equation, which has a quadratic nonlinearity [36]. The stochastic behavior of the amplitudes depends on the spatial modes that are included in the additive noise, with intermittent behavior explored for increasing noise coefficients. In [37], a multiple scale analysis was applied to stochastic DDEs to derive approximate stochastic equations for the amplitudes of oscillatory solutions near critical delays of deterministic systems. They show that the interaction of noise and delay support these oscillations, even over long time intervals.

Summary of results

In the absence of delay and noise, hence $a\tau = 0$ and $\tilde{\sigma} = 0$, the SHE has a basic state $u = 0$ which loses its stability to periodic spatial patterns with wavenumber $k = k_c = 1$ at the parameter value $r = r_c = 0$. For $r = r_c + \varepsilon^2 r_2$ with $\varepsilon \ll 1$, these patterns are modulated by an $O(\varepsilon)$ amplitude satisfying the real Ginzburg–Landau (GL) equation on a slow time scale $T = \varepsilon^2 t$ and a slow spatial scale $X = \varepsilon x$. There exist stationary periodic solutions to this Ginzburg–Landau that are stable in certain parameter ranges when the so-called Eckhaus criterion holds. In order to compare with these results, we first consider the SHE+P without noise near the primary instability of $u = 0$. A standard linear analysis of the

deterministic case with $\sigma = 0$ as performed in Section 2.1, gives a first indication of the important differences that arise due to the delayed feedback.

Result 2.1: *We conclude from the dispersion relation that for $a\tau < 1$ standing wave solutions (Turing patterns) arise with the critical wavelength $k_c = 1$ at the same critical value $r = r_c = 0$ as for the SHE without delay. Interestingly, we find for $a\tau > 1$ that traveling waves solutions occur at a different critical value for r which is negative.*

Note that traveling waves are not observed in the standard SHE. Our result agrees with those in [27] where r is fixed to $r = -1$ and traveling wave solutions are observed numerically for $a\tau > 1$. Other values for r are not considered in [27]. Focusing on the case $a\tau < 1$, we consider the asymptotic behavior of the eigenvalues via a linear analysis of the SHE+P.

Result 2.2: *For the choice $a\tau < 1$, and parameter values near the critical value r_c, hence $r = r_c + \epsilon^2 r_2$ with $\epsilon \ll 1$, we find that a new intermediate time scale $S = \epsilon t$ appears for $1 - a\tau = O(\epsilon)$.* This intermediate time scale also appears in the nonlinear analysis near r_c.

Result 2.4: *We derive a GL-type equation for the modulation of the Turing patterns that inherits terms of the Pyragas form on the long time scale.* We study the existence and stability of periodic solutions of this modulation equation. On the one hand, the results appear similar to that of the SHE, since the same Eckhaus stability criterion is found both with and without Pyragas control, and for $0 < 1 - a\tau = O(1)$, patterns evolve on the usual time scale $T = \epsilon^2 t$ as in the case without delay. On the other hand, for $a\tau$ near 1, differences appear in the evolution of the transients, with the intermediate time scale S appearing in the stability analysis of the periodic solutions to this equation.

Result 2.6: *The eigenvalues obtained via the linear stability analysis are complex for $1 - a\tau = O(\epsilon)$ and real for $1 - a\tau = O(1)$.* An implication of these differences are accelerated transitions to a stable Turing pattern for $1 - a\tau = O(\epsilon)$ and oscillations in these transitions, as indeed observed in the numerics. In other words, the amplitude equation inherits the Pyragas control, driving transient behavior to equilibrium on the S-time scale for $a\tau$ near 1. This resulting acceleration of transitions via delayed feedback can be a useful consideration in engineering feedback controls to achieve enhanced stability properties.

As far as we know this intermediate time scale and transient behavior have not yet been observed before in the literature. Even though stationary patterns are stable in the deterministic case for all $a\tau$ near 1, there are further implications of these oscillations, damped on the $O(\epsilon)$ time scale, in the presence of noise. For the analysis of the stochastic SHE+P, we consider (1.1) near the critical value of r, $r = r_c + \epsilon^2 r_2$ with an appropriate choice of $\tilde{\sigma} = \epsilon\sigma$, for which we expect to see non-trivial stochastic dynamics [28,33,36]. Writing the solution u in terms of spatial modes as suggested by the deterministic analysis and the noisy forcing, we use a multiple scale expansion of the amplitudes in terms of the time only.

Result 3.1: *We find that solutions for the stochastic SHE+P are well-approximated by a system composed of a Landau-type subsystem for the amplitude of the primary modes with wave number $k = \pm 1$ coupled to the amplitude of the zero mode (constant in space) described to leading order by a fast Ornstein–Uhlenbeck-type process. As in the deterministic case, the Pyragas control is also present in this reduced system.* The primary mode evolves on the slow time scale, while the amplitude of the zero mode evolves on the fast t time scale. Exploiting this difference in time scales, we use an averaging approach [38] to reduce the system further to an averaged equation for the amplitude of the primary mode, with nonlinear terms of the fast Ornstein–Uhlenbeck-type process approximated by their moments. This averaged amplitude equation can be analyzed as in the deterministic case, giving the stability of steady state solutions corresponding to a pattern (on average) for u with wave number $k = 1$.

Result 3.2: *The stability analysis of the averaged amplitude equations indicates how both the noise and the delay change the amplitude of the pattern, with the delay further increasing the noise-induced shift of the value of r above which these patterns are stable* [39]. As in the deterministic case, the stability analysis captures its complex eigenvalues of the underlying dynamics, indicating evolution on the time scale $T = \epsilon^2 t$ for $1 - a\tau = O(1)$ and, with complex eigenvalues on the scale $S = \epsilon t$ for $1 - a\tau = O(\epsilon)$. The observation that the averaged system has complex eigenvalues, motivates a second approach for studying the coupled system of amplitudes for the primary and zero modes. The spectral densities for these modes are studied via a linearization of the system about the stable pattern that is identified through the averaged amplitude equation.

Results 3.3: *We obtain analytical expressions for the spectral densities which compare well with the power spectral densities obtained numerically for the corresponding modes of the full system* (1.1).

Result 4.1: *Changes in the shape of the spectral density indicate interaction between the noisy fluctuations and the complex eigenvalues for $1 - a\tau = O(\epsilon)$, analogous to coherence resonance as observed in other systems where weakly damped oscillations of the deterministic system are sustained by noise.* Specifically, for $1 - a\tau = O(\epsilon)$ or smaller, the zero mode has a peak in its spectral density corresponding to the imaginary part of the complex eigenvalues. Moreover, the power spectrum of the primary mode has an $\mathcal{O}(\varepsilon)$-wide band of frequencies that do not decay, indicating a significant amount of autocorrelation on the S time scale. This behavior of spectral densities is contrasted with the case $1 - a\tau = O(1)$, where the spectral densities of all modes decay rapidly from $\omega = 0$ as observed for the case without Pyragas control $a\tau = 0$. This behavior is observed in both the analytical expressions and numerical results.

In this paper the stochastic SHE+P is simulated with a spectral method in space based on [40], combined with Euler–Maruyama time stepping [41] that incorporates an integrating factor for the non-delayed linear terms. In the deterministic case, a similar spectral method was used to simulate the dynamics of both the SHE+P and the amplitude equation in slow time and space. Power spectra were computed by centering the time series and applying the MatLab function `pwelch`.

Organization

In Section 2.1, we perform the linear stability analysis for the Swift–Hohenberg equation with Pyragas delay, where we derive the parameter regime for the Turing bifurcations, and show how a new S time scale appears in the modulations of the linearized equation for $a\tau$ close to 1, with technical details given in Appendices A and B. The derivation of the amplitude equation and its stability analysis is presented in Section 2.2. The stochastic case is treated in Section 3, where we derive the averaged amplitude equation as well as the approximate power spectra of the amplitudes. The latter uses some essential results for spectra of linear SDDEs which are detailed in Appendix D. We complement the analytical results with numerical simulations of both the SHE+P, with and without noise, and the derived amplitude equations. The results are shown in the figures throughout the paper and in Section 4 for the stochastic SHE+P.

2. Deterministic Swift–Hohenberg equation with Pyragas control

2.1. Linear stability analysis

We consider patterns described by the Swift–Hohenberg equation with Pyragas control (SHE+P)

$$\partial_t u = -(1 + \partial_x^2)^2 u + ru + a(u - u(t - \tau)) - u^3. \tag{2.1}$$

The nature of Pyragas control implies that the SHE+P has the same basic state $u = 0$ as the usual SHE. The critical differences that arise

due to the Pyragas control are the *type* of patterns that bifurcate from the basic state and the parameter values corresponding to these bifurcations. We start with the linear stability analysis of the basic state, motivating the appearance of temporal and spatial scales that are important in the evolution of these patterns.

Linearizing (2.1) about the basic state $u = 0$ yields

$$\partial_t u = -(1+\partial_x^2)^2 u + ru + a(u - u(t-\tau)). \tag{2.2}$$

We consider solutions $u = e^{ikx+\omega t}$ for (2.2) representing oscillatory patterns. This leads to the dispersion curve for the eigenvalue $\omega = \omega(k, r)$ describing the growth or decay of the solution,

$$\omega = -(1-k^2)^2 + r + a(1-e^{-\omega\tau}) =: \mu(k, r) + a(1-e^{-\omega\tau}). \tag{2.3}$$

In the absence of delay ($a\tau = 0$), it is readily seen that ω is real and unique, and the basic state loses its stability to a spatially periodic pattern with wave number $k_c = \pm 1$ when ω becomes positive at the critical value $r_c = 0$.

When we analyze equation (2.3) to include Pyragas control, we study the leading eigenvalue (the ω with largest real part) and denote this by ω_0. For this ω_0 we find that there are two distinct cases depending on the size of $a\tau$. We show that

Result 2.1. *The $Re(\omega_0)$ changes sign at the critical wave number $k_c = \pm 1$ and at the critical point r_c when:*

Case 1. *For $a\tau < 1$: the solution $u = 0$ becomes unstable at $r_c = 0$ and $\omega_0(k_c, r_c) = 0$; the solution undergoes a Turing bifurcation.*

Case 2. *For $a\tau > 1$: the solution $u = 0$ becomes unstable at $r_c = a(\cos(\nu_c\tau) - 1) < 0$ and $\omega_0(k_c, r_c) = \pm i\nu_c$, where $\nu_c \in (0, \frac{\pi}{\tau})$ satisfies $\nu_c = a\sin(\nu_c\tau)$. Then, the $u = 0$ solution undergoes a Turing–Hopf bifurcation.*

Derivation For $a\tau \neq 0$, the transcendental nature of (2.3) leads to infinitely many complex eigenvalues. The leading eigenvalue ω_0 with largest real part is expressed in terms of the Lambert function, W_0, as

$$\omega_0(k, r) = \mu(k, r) + a + \frac{1}{\tau} W_0(-a\tau e^{-(a+\mu(k,r))\tau}), \tag{2.4}$$

see Appendix A. Next, we look for the critical value $r = r_c$ for which $Re(\omega_0)$ first becomes positive at some critical wave number k_c. Then, separating the real and imaginary parts of (2.4), as in Appendix A.1, yields the result.

Result 2.1 indicates a Turing bifurcation for $0 < a\tau < 1$, in which the basic state loses stability to a stationary periodic pattern as in the SHE without delay, with wave number $k_c = \pm 1$ at the bifurcation value $r_c = 0$. For $a\tau > 1$, the basic state loses stability to traveling wave patterns (indicating a Turing–Hopf bifurcation) also with the wave number $k_c = \pm 1$ but at a different bifurcation value $r_c < 0$. Thus we see an essential difference between the SHE+P and the SHE, in that the delay can cause a shift in bifurcation and generate traveling waves in the SHE+P not observed in the SHE.

In [27], the dispersion relation (2.3) and expression (2.4) were also found. However, after that the authors fix $r = -1$ and plot the region of stability numerically in the (α, τ)-plane with stability boundary $\alpha\tau = 1$. This choice of r then yields complex eigenvalues and traveling wave solutions in the numerical simulations.

Henceforth in this paper, we only consider the Turing bifurcation, $a\tau < 1$. Next, we analyze the asymptotic behavior of ω_0 for values of the parameters r, k near their critical values $r_c = 0$, $k_c = 1$, this leads to

Result 2.2. *For*

$$r = \varepsilon^2 r_2, \quad k = 1 + \varepsilon K, \quad \text{where } \varepsilon \ll 1, \tag{2.5}$$

the asymptotic behavior of ω_0 is given by

$$\omega_0 = \begin{cases} \mathcal{O}(\varepsilon), & \text{if } 1 - a\tau = \mathcal{O}(\varepsilon) \\ \mathcal{O}(\varepsilon^{1+\kappa}), & \text{if } 1 - a\tau = \mathcal{O}(\varepsilon^{1-\kappa}) \text{ with } 0 < \kappa \leq 1. \end{cases} \tag{2.6}$$

Remark 2.3. The behavior of ω_0 motivates the appearance of dynamics on a *new time scale* $S = \varepsilon t$ faster than $T = \varepsilon^2 t$ in the case when $1 - a\tau = O(\varepsilon)$. As shown in Fig. 1, for $a\tau$ near 1, the dispersion curve is elliptical for $|k - 1| = O(\varepsilon)$ corresponding to $\omega = \mathcal{O}(\varepsilon)$ and the growth of the instability is on the $S = \varepsilon t$ time scale. For $1 - a\tau = O(1)$ the dispersion curve is locally quadratic near $k = 1$ with $\omega_0 = \mathcal{O}(\varepsilon^2)$ and the growth of the instability is on the T time scale.

Fig. 1 also illustrates that $Re(\omega_0)$ is non-differentiable at the value of k where $Re(\omega_0(k, \varepsilon^2 r_2)) = \frac{1}{\tau}\ln(a\tau)$, see Appendix A. This value is significant for $Im(\omega_0)$, since for $Re(\omega_0) > \frac{1}{\tau}\ln(a\tau)$, ω_0 is real and otherwise it is complex. The non-differentiability produces a pronounced "bubble" near $k = 1$ for $a\tau \ll 1$.

Derivation of Result 2.2. For $a\tau = 0$, it follows that $Re(\omega) = O(\varepsilon^2)$ [42], corresponding to evolution of the pattern on a slow time scale $T = \varepsilon^2 t$ as reflected in the well-known derivation of the amplitude equation for bifurcating Turing patterns. For $a\tau \neq 0$ we again use (2.5) and find that $\omega_0(1 + \varepsilon K, \varepsilon^2 r_2) = O(\varepsilon^\gamma)$ where $1 \leq \gamma \leq 2$ depends on the magnitude of $1 - a\tau$. Heuristically, we can see this by assuming that $\omega_0 \ll 1$ in (2.3). Expanding the exponential term around $\omega_0 = 0$, we find

$$0 \sim \varepsilon^2(r_2 - 4K^2) - (1 - a\tau)\omega_0 - \frac{a\tau^2}{2}\omega_0^2. \tag{2.7}$$

From (2.7) we see that if $1 - a\tau = O(1)$ then $\omega_0 = \mathcal{O}(\varepsilon^2)$ and if $1 - a\tau = \mathcal{O}(\varepsilon)$, then $\omega_0 = \mathcal{O}(\varepsilon)$. These results are demonstrated in detail in Appendix B, using expansions of the Lambert function W_0 where the final result follows from (B.3).

The linear analysis indicates that the delay is important for the creation of new time scales that do not occur without delay, but the linearized equation does not capture the nonlinear behavior and stability of the Turing patterns. To describe the dynamics of these patterns, including contributions on the S and T time scales, we derive the amplitude equations for stationary periodic patterns in the next section.

2.2. Amplitude equation for the deterministic Swift–Hohenberg equation with Pyragas control

In this section we derive, for the deterministic SHE+P (2.1), an amplitude equation that describes the modulation on slow time and space scales for the unstable mode $e^{\pm ix}$ close to the bifurcation, with $r = \varepsilon^2 r_2$ for $\varepsilon \ll 1$. We assume an asymptotic expansion of the solution taking the form

$$u(x, t) = \varepsilon v_1 + \varepsilon^2 v_2 + \varepsilon^3 v_3 + \cdots \tag{2.8}$$
$$v_1(x, X, t, T) = A(X, T)e^{ix} + \text{c.c.}$$

where c.c. indicates complex conjugate and the amplitude $A(X, T)$, which depends on slow spatial and temporal scales X and T, is to be determined. Following from the linear analysis (2.2)–(2.6), v_1 is precisely the solution to

$$\mathcal{S}v := \partial_t v + (1 + \partial_x^2)^2 v - a(v - v(t-\tau)) = 0 \tag{2.9}$$

where $\mathcal{S}$ is the linearized operator of the SHE+P at the critical value $r_c = 0$. Near this critical value we expect evolution on the slow spatial scale $X = \varepsilon x$ and slow temporal scale $T = \epsilon^2 t$ for $1 - a\tau = O(1)$.

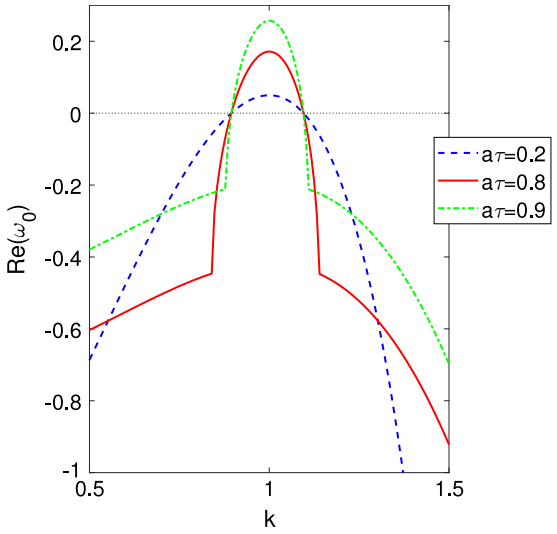

Fig. 1. Dispersion curves for the Turing bifurcation case, $a\tau < 1$, with $\varepsilon = 0.2$, $r_2 = 1$ and three sets of delay parameters: $a = 0.4$, $\tau = 0.5$, where $1 - a\tau = \mathcal{O}(1)$ (dashed blue curve), and $a = 1.6$, $\tau = 0.5$ (red curve) and $a = 1.8$, $\tau = 0.5$ (green curve), both with $1 - a\tau \ll 1$. For all $0 \le a\tau < 1$, $Re(\omega_0)$ is positive on the same $\mathcal{O}(\varepsilon)$ band of wavenumbers for which $\mu(k, r) := -(1 - k^2)^2 + r$ is positive. For $a = 1.6$ or $a = 1.8$ and $\tau = 0.5$, $Re(\omega_0)$ is non-differentiable at the value of k where $Re(\omega_0(k, \varepsilon^2 r_2)) = \frac{1}{\tau}\ln(a\tau)$. (For interpretation of the references to color in this figure legend, the reader is referred to the web version of this article.)

Result 2.4. *We obtain the amplitude equation for A via a multiple scales analysis,*

$$A_T = 4\partial_X^2 A + r_2 A - 3A|A|^2 + a\varepsilon^{-2} \times \big(A(X,T) - A(X, T - \varepsilon^2\tau)\big). \tag{2.10}$$

This is simply the Ginzburg–Landau equation with a Pyragas term on the T time scale.

Note that even though the Pyragas term has an ϵ^2 in it, this term is $O(1)$, as discussed in the derivation of Result 2.4 below. So this term balances with the rest of the terms and thus appears in the amplitude equation.

Derivation of Result 2.4. As indicated in Remark 2.3, there are several possibilities for slow time scales: either $S = \varepsilon t$ for $1 - a\tau = O(\varepsilon)$ or $T = \varepsilon^2 t$ for $1 - a\tau = O(1)$. Moreover, for $1 - a\tau = O(\varepsilon^{1-\kappa})$, $0 < \kappa \le 1$, the time scale is $T_\kappa = \varepsilon^{1-\kappa} t$, an intermediate time scale connecting the other two time scales. As we see below, it is not necessary to track this "intermediate" time scale, so we only take into account T and S. A standard multiple scale analysis of (2.1) can then be used to find the evolution equation for the amplitude A for the two different time scales that depend on the order of magnitude of $1 - a\tau$. However, for both cases we find that the amplitude equation has exactly the same form, with the only difference a factor of ε in the linear terms, corresponding to $T = \varepsilon S$. The magnitude rather than the form of the linear terms, including the Pyragas terms, depends on the size of $1 - a\tau$, as follows directly from (2.6), demonstrating the emergence of different time scales in the linear growth. In contrast, the separate multiple scale analyses show that stabilization via the nonlinear terms appears at the same order regardless of the magnitude of $1 - a\tau$. Therefore, for simplicity we take $A(X, T)$ and we take $v_i = v_i(x, X, t, T)$, completing the multiple scale analysis with time scale $T = \varepsilon^2 t$ only. In Remark 2.5 below we point out where the scale S may appear in the dynamics of u, and how it is accommodated in our analysis.

In the following, we use the shorthand $\frac{\partial}{\partial x} \to \partial_x$ and similarly for X, t and T. As is typical in the multiple scales approach, the slow and fast variables are treated as independent from each other, we have

$$\frac{d}{dt} = \partial_t + \varepsilon^2\partial_T, \tag{2.11}$$
$$\frac{d}{dx} = \partial_x + \varepsilon\partial_X,$$
$$\big(v_i(x, X, t, T) - v_i(x, X, t - \tau, T - \varepsilon^2\tau)\big) = \big(v_i(x, X, t, T) - v_i(x, X, t - \tau, T)\big) + \varepsilon^2\left(\frac{v_i(x, X, t - \tau, T) - v_i(x, X, t - \tau, T - \varepsilon^2\tau)}{\varepsilon^2}\right).$$

We treat the term

$$\left(\frac{v_i(x, X, t - \tau, T) - v_i(x, X, t - \tau, T - \varepsilon^2\tau)}{\varepsilon^2}\right) \tag{2.12}$$

as $\mathcal{O}(1)$. This follows from a Taylor expansion of the second term in this expression and the fact that $\partial_T v_i = O(1)$ as is consistent with the behavior considered in this section. Note that here we keep the delay term (2.12) in the equation and do not replace it with $\partial_T v_i$. Keeping the delay terms in the equations facilitates comparisons below to the stability analysis of Section 2.1 and to results for the averaged equations in Section 3.

Using (2.11), the 4th order partial differential operator is

$$-\left(1 + \frac{\partial^2}{\partial x^2}\right)^2 = -(1 + \partial_x^2)^2 - 4\varepsilon(1 + \partial_x^2)\partial_x\partial_X - 2\varepsilon^2\left(2\partial_x^2\partial_X^2 + (1 + \partial_x^2)\partial_X^2\right) - 4\varepsilon^3\partial_x\partial_X^3 - \varepsilon^4\partial_X^4 = \mathcal{L}_0 + \varepsilon\mathcal{L}_1 + \varepsilon^2\mathcal{L}_2 + \varepsilon^3\mathcal{L}_3 + \varepsilon^4\mathcal{L}_4.$$

To further simplify notation, arguments that are not delayed, that is (x, X, t, T), are not specified. For example, $v_1(t-\tau) = v_1(x, X, t-\tau, T)$.

Next, we substitute the asymptotic expansion (2.8) into (2.1) and collect the coefficients of the powers of ε, to find

$$\mathcal{O}(\varepsilon^1): \quad \mathcal{S}v_1 = 0, \tag{2.13}$$
$$\mathcal{O}(\varepsilon^2): \quad \mathcal{S}v_2 = \mathcal{L}_1 v_1, \tag{2.14}$$
$$\mathcal{O}(\varepsilon^3): \quad \mathcal{S}v_3 = \mathcal{L}_1 v_2 - \partial_T v_1 + r_2 v_1 + \mathcal{L}_2 v_1 + a\varepsilon^{-2}\big(v_1(t-\tau) - v_1(t-\tau, T - \varepsilon^2\tau)\big) - v_1^3. \tag{2.15}$$

We already chose v_1 to satisfy (2.8), hence $\mathcal{S}v_1 = 0$. Also, $\mathcal{L}_1 v_1 = 0$, so that $\mathcal{S}v_2 = 0$ in (2.14). Since $\mathcal{S}v_2 = 0$, we could conclude that $v_2 = v_1$. This choice would lead to two terms at different with the same form, so for simplicity they can be combined without loss of generality. Consequently, we take $v_2 = 0$. Then Eq. (2.15) at $\mathcal{O}(\varepsilon^3)$ becomes

$$\mathcal{S}v_3 = -\partial_T v_1 + r_2 v_1 + \mathcal{L}_2 v_1 + a\varepsilon^{-2}\big(v_1(t-\tau) - v_1(t-\tau, T - \varepsilon^2\tau)\big) - v_1^3. \tag{2.16}$$

We invoke a solvability condition for the existence of a smooth solution with sublinear growth. Essentially, this condition requires that terms on the right-hand side (RHS) of (2.16) must be orthogonal to $e^{\pm ix}$ which is in the null space of the adjoint of $\mathcal{S}$. (See Appendix C.) Applying this condition to (2.16) yields

$$\lim_{t_0\to\infty}\frac{1}{t_0}\int_0^{t_0}\int_{\mathbb{R}}[-\partial_T v_1 + r_2 v_1 + \mathcal{L}_2 v_1 + a\varepsilon^{-2}\big(v_1(t-\tau) - v_1(t-\tau, T-\varepsilon^2\tau)\big) - v_1^3]e^{\pm ix}\,dx\,dt = 0.$$

Treating the slow scales X and T as independent of x and t, we obtain Result 2.4.

Remark 2.5. While we have derived this equation in terms of the slow time scale $T = \varepsilon^2 t$, we note that it captures evolution on the $S = \varepsilon t$ scale as well. This observation follows from the linear terms in (2.10) that have exactly the same form as the linearized SHE+P in (2.2). The eigenvalues associated with these terms indicate that the solution evolves on the S scale for $1 - a\tau = O(\varepsilon)$ or smaller (2.6). We could have included this extra time scale in our derivation of the amplitude equation, which leads to the appearance of additional terms of the form

$$\left(-A_S + a\varepsilon^{-1}(A - A(S - \varepsilon\tau))\right) e^{ix} + c.c. \tag{2.17}$$

in (2.14) at $O(\varepsilon^2)$. Since these are not sufficient to describe the nonlinear evolution of the amplitude A, the terms from the $O(\varepsilon^3)$ Eq. (2.15) are needed to complete the derivation. Besides the nonlinear terms, linear terms of the same form as (2.17) appear at $O(\varepsilon^3)$, corresponding to the T scale. Since the linear terms have the same form at both $O(\varepsilon^2)$ and $O(\varepsilon^3)$, from the multiple scale perspective these can be combined in terms of just one time scale. Even though the S time scale does not appear explicitly in (2.10), this time scale does appear in the stability analysis and stochastic dynamics considered below for $1 - a\tau \ll 1$.

2.3. Stability analysis for the deterministic amplitude equation

The stability of patterns in the SHE+P is seen through the stability analysis of solutions of the amplitude equation (2.10). Steady periodic solutions of (2.10) are given by

$$A(X) = \rho_0 e^{i(KX+\phi_0)} \text{ for } 3\rho_0^2 = r_2 - 4K^2, \tag{2.18}$$

with wave number K and arbitrary constant phase shift ϕ_0. Combined with (2.8), this result gives standing wave solutions usually known as rolls in the SHE context. We study the linear stability of these solutions by writing

$$A(T, X) = (\rho_0 + \rho(T, X))e^{i(KX+\phi(T,X))} \tag{2.19}$$

and consider the stability of modes $e^{i\nu X}$ by using

$$\begin{pmatrix} \rho \\ \rho_0\phi \end{pmatrix} = \begin{pmatrix} \gamma_1 \\ \gamma_2 \end{pmatrix} e^{i\nu X + \Omega T} \tag{2.20}$$

Result 2.6. *The stability of rolls (2.19) is given by non-trivial eigenvalues Ω satisfying*

$$\Omega - a\varepsilon^{-2}(1 - e^{-\Omega\varepsilon^2\tau}) = \left(-(4\nu^2 + 3\rho_0^2) \pm \sqrt{9\rho_0^4 + 64\nu^2K^2}\right) := h_\pm(\nu, K, \rho_0) \tag{2.21}$$

where $h_\pm(\nu, K, \rho_0)$ is real, and $h_- < h_+$. The condition $h_\pm < 0$ for $0 < a\tau < 1$ is

$$r_2 > 12K^2, \tag{2.22}$$

is the well-known Eckhaus stability criterion [43] observed for $a\tau = 0$. Furthermore, both real and complex Ω arise for $a\tau \neq 0$, as obtained from a calculation analogous to the derivation of (2.6). This observation is in contrast to the case $a\tau = 0$, where the same linear stability analysis yields real eigenvalues.

Derivation of Result 2.6. We study the linear stability of (2.18) for $a\tau > 0$, using (2.19), with $\rho(T, X) \ll 1$ and $\phi(T, X) \ll 1$. Substituting this expression into (2.10), linearizing about $\rho = \phi = 0$ and splitting into complex and real parts, yields

$$\rho_T = 4\rho_{XX} - 8\rho_0 K\phi_X - 6\rho_0^2\rho + a\varepsilon^{-2}(\rho - \rho(T - \varepsilon^2\tau)) \tag{2.23a}$$

$$\rho_0\phi_T = 4\rho_0\phi_{XX} + 8K\rho_X + a\varepsilon^{-2}\rho_0(\phi - \phi(T - \varepsilon^2\tau)). \tag{2.23b}$$

Substituting (2.20) into (2.23), and solving for Ω yields Result 2.6.

To highlight the appearance of complex eigenvalues, we compare (2.21) with (2.3) obtained in the linear stability analysis of the basic state $u = 0$. The eigenvalue Ω solves the same type of transcendental equation. A heuristic argument, based on an asymptotic expansion of (2.21) similar to that used to obtain (2.7) for ω, yields the following equation for $\Omega \ll 1$

$$0 \sim h_\pm - (1 - a\tau)\Omega - \frac{a\tau^2}{2}(\varepsilon\Omega)^2. \tag{2.24}$$

Details for the behavior of Ω are given in Appendix B as discussed following (B.3).

Fig. 2 illustrates the different time scales in the evolution toward a stable pattern for different values of $1 - a\tau$, as captured by the behavior of the eigenvalues in (B.3). On the left we plot the evolution of A obtained from the amplitude equation (2.10) for several values of a, fixing other parameters. On the right we give the real parts of ω_0 and $\varepsilon^2\Omega$ as functions of $a\tau$, for various choices of ε. For the last case in (B.3) where $0 < a\tau < 1$ and $1 - a\tau = \mathcal{O}(1)$, we find that $\Omega = O(1)$, and $Re(\Omega) < 0$ for $h_\pm < 0$. Then the evolution to the stable equilibrium value $A = \rho_0$ is on the time scale T. However, for $1 - a\tau = \mathcal{O}(\varepsilon)$, $\Omega = \mathcal{O}(\varepsilon^{-1})$. Since $Re(\Omega)$ represents the decay rate on the T time scale, this behavior reflects the evolution of the solution of the SHE+P on the $S = \varepsilon t$ time scale for $1 - a\tau = O(\varepsilon)$, as discussed in Remark 2.3 in Section 2.1. Hence, the amplitude evolves faster to $A = \rho_0$ as observed for $a\tau \geq 0.5$ in Fig. 2(left). Furthermore, if $1 - a\tau < \sqrt{2\tau|h_\pm|}\varepsilon$ and $h_\pm < 0$, then Ω is complex, and there are transient oscillations in the amplitude's behavior as can be seen for larger values of a in Fig. 2(left). Note that this is in contrast to (2.7) which has two real roots.

For values of $a\tau$ even closer to 1, that is, $1 - a\tau = \mathcal{O}(\varepsilon^{1+\kappa})$ for $\kappa > 0$, Ω is also complex and the oscillations are more prominent in the evolution of A, as shown in Fig. 2(left) for $a\tau = 0.8$ and $a\tau = 0.9$. For $a\tau = 0.9$, we also compare the time evolution of the amplitude obtained from the amplitude equation (2.10) to the amplitude of the $k = 1$ mode obtained numerically from the full SHE+P(2.1). This more prominent oscillatory behavior follows from the fact that $Im(\Omega) = O(\varepsilon^{-1})$ and $Re(\Omega) = o(\varepsilon)$, with the oscillations damped on an ever slower time scale when $a\tau$ is closer to 1. Thus, although the Pyragas control does not change the stability of the steady patterns, it does change the evolution of the amplitude, exhibiting faster transitions to values near the steady state $A = \rho_0$ and oscillations in these transients.

Fig. 3 shows results from the simulation of the full SHE+P, based on a Fourier representation, that illustrate the Eckhaus instability for this system. We plot the magnitude of the Fourier coefficients of the solution versus their corresponding wave numbers. The initial condition is of the form (2.19) used in the stability analysis, $2\varepsilon(\rho_0 + \rho)\cos(x + KX)$, with ρ_0 and K related through (2.18). For a given ρ_0 and ρ, on the left we show results for K satisfying the stability condition (2.22) (left); hence patterns with wave number $1 + \epsilon K$ maintain that wave number. Then the corresponding non-zero coefficient evolves to the stable value of the amplitude, and the Fourier coefficients that were zero in the initial condition remain zero. On the right, we choose a larger value of K, so that the initial condition violates the stability condition (2.22). Then the pattern evolves to one that does satisfy this condition.

3. Stochastic Swift–Hohenberg equation with Pyragas control

We now consider the stochastic SHE+P driven by additive time-dependent noise

$$du = \left[-(1 + \partial_x^2)^2 u + \varepsilon^2 r_2 u - u^3 + a(u - u(t - \tau))\right] dt + \varepsilon\sigma dB(t), \tag{3.1}$$

with $B(t)$ a standard Brownian motion for simplicity, since that is sufficient for our focus on the temporal modulations of patterns

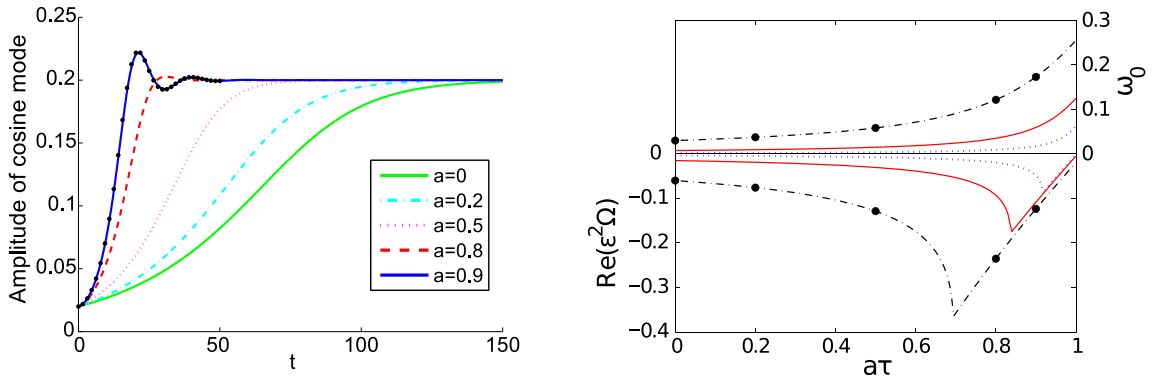

Fig. 2. Indication of complex eigenvalues and intermediate time scale S in the amplitude dynamics for $a\tau$ near 1. For both panels $\tau = 1$, $r_2 = 3$, and for simplicity we show the case without spatial modulation $\nu = K = 0$, noting that similar results (not shown) are observed for ν and K non-zero. Left: Evolution of A obtained from the amplitude equation (2.10) for several values of a, for $\varepsilon = 0.1$. For $a\tau = 0.9$, the black dots indicate the amplitude of the $k = 1$ mode obtained from the numerical solution of (2.1), scaled with ε. Right: Real parts of ω_0 and $\varepsilon^2\Omega$ as functions of $a\tau$, for $\varepsilon = 0.025$ (blue dotted line), $\varepsilon = 0.05$ (red solid line) and $\varepsilon = 0.1$ (black broken line). For all $0 \le a\tau < 1$, ω_0 is real and positive for $r_2 > 0$. $Re(\varepsilon^2\Omega) < 0$ since (2.22) is satisfied. Analogous to the behavior of ω in Fig. 1, $Re(\varepsilon^2\Omega)$ is non-differentiable at values of $a\tau$ where $2r_2\varepsilon^2 = \left|\frac{1}{\tau}(\ln(a\tau) + 1 - a\tau)\right|$, with Ω real (complex) for $a\tau$ below (above) this value of $a\tau$. The black dots on the curve for $\varepsilon = 0.1$ correspond to the values of $a\tau$ used in the left panel. (For interpretation of the references to color in this figure legend, the reader is referred to the web version of this article.)

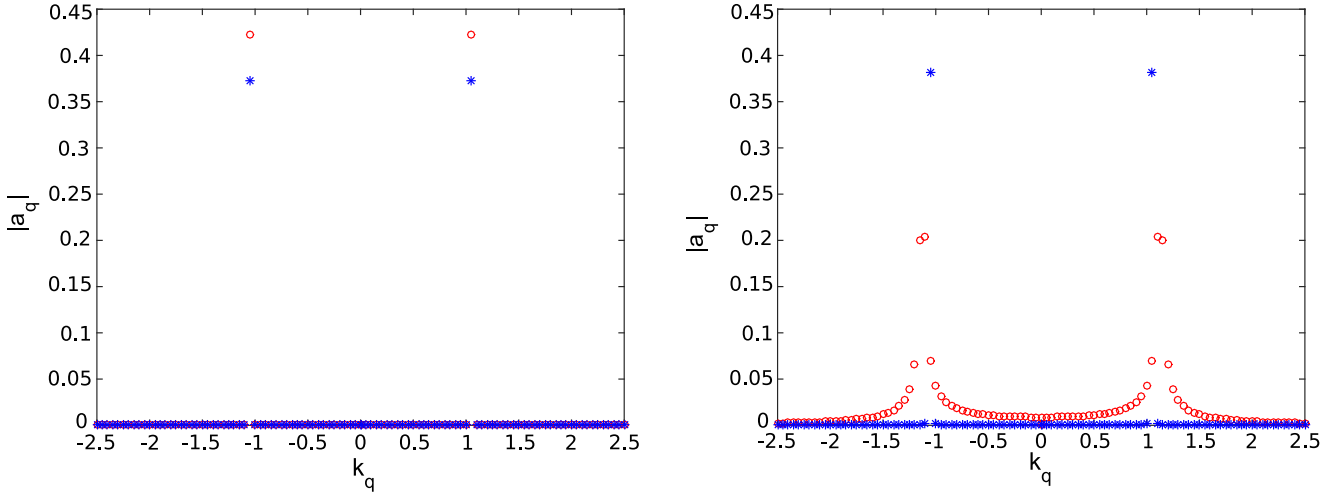

Fig. 3. In both figures we show the magnitude of the coefficients $|a_q|$ versus k_q in the approximation for $u(x,t) \approx \sum_q a_q e^{ik_q x}$ for $a = 0.9$, $\tau = 1$, $r_2 = 3$, $\varepsilon = 0.2$. Initial conditions take the form $2\varepsilon(\rho_0 + \rho)\cos(x + KX)$ as in (2.19), with ρ_0 and K related through (2.18) and $\rho = 0.1$. Red circles indicate $|a_q|$ at $t = 0$, and blue stars $*$'s indicate $|a_q|$ after long times. Left: The value of $K = 0.25$ satisfies the stability criterion (2.22), so that non-zero values of a_q corresponding to $|k_q| = 1.05$ evolve to the stable value approximated by (2.18) as $2\varepsilon\rho_0 \approx 0.38$, while the remaining $a_q = 0$ for all time. Right: The value of $K = 0.625$ violates the stability criterion (2.22), so patterns evolve to the stable pattern observed in the left panel. With different initial perturbations the system can evolve to other stable patterns (not shown) (For interpretation of the references to color in this figure legend, the reader is referred to the web version of this article.)

due to the interplay between noise and delay. As in Section 2 we take $a\tau < 1$, where Turing patterns are observed for $r_2 > 0$. We take $r = \epsilon^2 r$ as motivated by the results in Section 2.2 and $\tilde{\sigma} = \epsilon\sigma$, $\sigma = O(1)$ in (1.1). Nontrivial stochastic pattern dynamics have been demonstrated for this scaling choice in a number of previous studies [28,33,36]. For noise coefficients that are an order of magnitude larger, the noise dominates the dynamics, while for noise coefficients that are smaller, the noise is essentially a small perturbation to the dominant regular pattern. Then we expect stochastic behavior involving the critical spatial mode as in v_1 (2.8), and we write the solution of (3.1) in a basis expansion, $u(x,t) = \sum_{k=-\infty}^{\infty} u_k e_k(x)$, where

$$e_0(x) \equiv 1, \qquad e_k(x) = \cos(kx),$$
$$e_{-k}(x) = \sin(kx), \qquad \text{for } k \in \mathbb{N}.$$

As shown in Section 2, the modes $e_{\pm 1}(x)$ are the critical modes appearing in the Turing pattern for $r_2 > 0$. In general we would expect the coefficients u_k to depend on fast and slow time scales as well as a long spatial scale, that is, $u_k(X, T, t)$. To focus on temporal modulations of the dominant pattern, we restrict our attention to $u_k(T, t)$, as in the ansatz below (3.2). Note that with the choice of $B(t)$, the noise appears in a single non-critical mode e_0. We anticipate that extensions are straightforward for finite dimensional space–time noise that does not act on the critical modes $e_{\pm 1}(x)$.

For $a\tau = 0$, the solution is known to be well-approximated by a slowly varying temporal modulation of the dominant pattern coupled to a fast Ornstein–Uhlenbeck (OU) process in the zero mode [31,32,36]. For $0 < a\tau < 1$, we expect similar behavior, where small solutions of (3.1) are well-approximated by

$$\varepsilon\left(A_1(T)\cos x + A_{-1}(T)\sin x + A_0(t)\right). \tag{3.2}$$

Then, we can derive a system of time-dependent amplitude equations for A_0 and $A_{\pm 1}$ resulting in

Result 3.1. *The dynamics of the relevant modes $A_{\pm 1}$ and A_0 in the approximation (3.2) of u are described by the truncated system of*

amplitude equations

$$dA_i = \Big[a\varepsilon^{-2}\big(A_i - A_i(T-\varepsilon^2\tau)\big) + (r_2 - 3A_0^2)A_i - \frac{3}{4}A_i\big(A_1^2 + A_{-1}^2\big)\Big]\,dT \qquad i = \pm 1, \tag{3.3a}$$

$$dA_0 = \Big[-\lambda_0 A_0 + a\big(A_0 - A_0(t-\tau)\big) + \varepsilon^2(r_2 - \frac{3}{2}(A_1^2 + A_{-1}^2))A_0 - \varepsilon^2 A_0^3\Big]\,dt + \sigma\,dB(t). \tag{3.3b}$$

Note that we have written the equation for A_0 on the fast time scale t and the equation for A_i, $i = \pm 1$ on the slow time scale T, since this form explicitly highlights that the amplitudes evolve on different time scales. The analysis of the derivation and in the following subsections is relatively straightforward with the equations in this form.

Derivation To derive the amplitude equations for $r = \varepsilon^2 r_2$, we use the following ansatz for u

$$u(x,t) = \varepsilon V(x,t) := \varepsilon\Big[A_1(T)\cos x + A_{-1}(T)\sin x + A_0(t,T) + \sum_{|k|\geq 2} A_k(t,T)e_k(x)\Big]. \tag{3.4}$$

This ansatz is motivated by results from the deterministic case, as well as the type of the noise in the forcing. Substituting u into (3.1) and considering the terms with coefficient $e_1(x) = \cos x$, we get

$$dA_1(T)\cos(x) = \cos(x)\Big[\varepsilon^2 r_2 A_1(T) - \varepsilon^2\mathcal{P}_1\big(V^3\big) + a\varepsilon^2\left(\frac{A_1(T) - A_1(T-\varepsilon^2\tau)}{\varepsilon^2}\right)\Big]\,dt\,. \tag{3.5}$$

Here $\mathcal{P}_k$ is the projection onto e_k under the inner product,

$$\mathcal{P}_k w = \frac{1}{\pi}\langle w, e_k\rangle = \frac{1}{\pi}\int_{-\pi}^{\pi} w\, e_k\, dx\,.$$

The first term in equation (3.1) cancels, for the same reasons that $\mathcal{S}v_1 = 0$ in (2.13) since A_1 is treated as a function of the slow time T, and thus constant relative to t. As in Section 2, we treat $\varepsilon^{-2}\big(A_1(T) - A_1(T-\varepsilon^2\tau)\big)$ as $O(1)$, for $0 < \epsilon^2 \ll 1$. Projecting (3.5) onto e_1 and replacing $t = \varepsilon^2 T$, we obtain an evolution equation on the slow time T,

$$dA_i(T) = \big[a\varepsilon^{-2}\big(A_i(T) - A_i(T-\varepsilon^2\tau)\big) + r_2 A_i(T) - \mathcal{P}_i\big(V^3\big)\big]\,dT, \tag{3.6}$$

where $i = 1$ and the Pyragas term has been rewritten as in (2.11). A similar result follows from substituting u into (3.1) and projecting the terms with coefficient $e_{-1}(x) = \sin x$ onto e_{-1} resulting in (3.6) with $i = -1$. Thus, $A_{\pm 1}$ evolves on the slow time scale $T = \varepsilon^2 t$.

Next, for the non-critical modes, substituting and projecting onto e_k, $k \neq \pm 1$ yields

$$dA_k = \big[(-\lambda_k A_k + a(A_k - A_k(t-\tau))) + \varepsilon^2 r_2 A_k - \varepsilon^2\mathcal{P}_k\big(V^3\big)\big]\,dt + \delta_{0k}\sigma\,dB(t), \tag{3.7}$$

where $\lambda_k > 0$ is the $O(1)$ eigenvalue for the partial differential operator $(1 + \partial_x^2)^2 e_k = \lambda_k e_k$ and $\delta_{ij} = 1$ if $i = j$, and otherwise vanishes. In these equations, the leading order linear terms do not cancel and the nonlinear terms give a small, higher order contribution, so that A_k for $k \neq \pm 1$ evolves on the fast time scale t. For $k = 0$, A_0 satisfies a stochastic differential delay equation (SDDE). In contrast, the contributions from A_k with $|k| \geq 2$ are negligible, with $\lambda_k > 0$ providing strong damping on the t time scale of contributions from the nonlinear terms $\varepsilon^2\mathcal{P}_k(V^3)$. Therefore, for $\varepsilon \ll 1$, we neglect contributions of A_k for $|k| \geq 2$ in the equations for $A_{\pm 1}$ and A_0 and consequently in the approximation of u in (3.4) this yields the result.

Next, we provide two complementary stochastic analyses that reveal the long time dynamics of these amplitudes. First, we derive from system (3.3) an averaged amplitude equation that describes the mean statistics of the approximate solution, based on A_0 approximated by a fast OU-type process. Second, we derive an approximation of the power spectrum from a linearized approximation and corresponding spectral analysis. For $a\tau$ near 1, both of the analyses indicate how the presence of noise sustains the S time scale dynamics over long times, in contrast to smaller values of $a\tau$ in which the evolution is primarily on the T time scale.

3.1. Averaging

We provide a formal approximation of the averaged amplitude equation for $A_{\pm 1}$, based on finding the approximate conditional stationary probability for the fast variable A_0 conditioned on a constant value of the slow variable $A_{\pm 1}$. This approach is analogous to the standard averaging approach of [38], but here we apply the approach using a multiple scales perspective for $0 < \varepsilon \ll 1$ rather than in the limit as $\varepsilon \to 0$.

We introduce a random variable $Z \sim A_0$, where the dynamics of Z are given by the linearized equation for A_0, that is, neglecting the term $\varepsilon^2 A_0^3$,

$$dZ = \big[-\Lambda(A_{\pm 1})Z + a\big(Z - Z(t-\tau)\big)\big]\,dt + \sigma\,dB(t), \tag{3.8}$$

$$\Lambda(A_{\pm 1}) = \lambda_0 - \varepsilon^2(r_2 - \frac{3}{2}(A_1^2 + A_{-1}^2)). \tag{3.9}$$

For $A_{\pm 1}$ constant, Z is an Ornstein–Uhlenbeck-type process with Pyragas control. It was shown in [44] that the stationary density $p(Z|A_{\pm 1})$ is a centered Gaussian with variance $\Sigma^2(\Lambda)$ given in Appendix D in expression (D.2). While in general $\Sigma(\Lambda)$ depends on $A_{\pm 1}$ through Λ, we can approximate $\Sigma(\Lambda)$ for the cases of interest where $A_{\pm 1}$ spends long periods of time near a steady state with high probability. Specifically, for parameter values where the amplitude is near a constant steady state, we approximate $\Sigma^2 = \Sigma^2(\lambda_0) + O(\varepsilon^2)$, with details given in Appendix D.

When we average Eq. (3.3a) for $A_{\pm 1}$ with respect to $p(Z|A_{\pm 1})$, we obtain

Result 3.2. *The averaged approximation $\mathcal{A}_{\pm 1}$ satisfies*

$$\frac{d\mathcal{A}_i}{dT} = a\varepsilon^{-2}(\mathcal{A}_i - \mathcal{A}_i(T-\varepsilon^2\tau)) + (r_2 - 3\Sigma^2(\Lambda))\mathcal{A}_i - \frac{3}{4}\mathcal{A}_i(\mathcal{A}_1^2 + \mathcal{A}_{-1}^2) \tag{3.10}$$

for $i = \pm 1$. The steady states of (3.10) are $(A_1, A_{-1}) = (2\rho_0, 0)$ and symmetrically $(A_1, A_{-1}) = (0, 2\rho_0)$, with the value of ρ_0 given by

$$3\rho_0^2 = r_2 - 3\Sigma^2(\lambda_0) + O(\varepsilon^2), \tag{3.11}$$

where $\Sigma^2(\Lambda)$ is given in expression (D.2).

As in the case without the Pyragas term [33], the averaged amplitude equation (3.10) does not include a noise term, and is independent of the process Z.

Comparing with the results in Section 2.3, we see that the value of $3\rho_0^2$ is shifted from r_2 to $r_2 - 3\Sigma^2$ through the influence of the noise. If we analyze the stability of the steady solution of (3.10), as was done for (2.10), we expect that on average for $r_2 > 3\Sigma^2$ a steady pattern with amplitude ρ_0 and wave number $k = 1$ is observed. For $r_2 < 3\Sigma^2$, we expect to see that the average of the amplitude of such a pattern vanishes on the long time scale. Thus there is a shift in the critical value r_c above which the (average)

Table 1
For parameters $\tau = 1, r_2 = 3, \varepsilon = 0.1, \sigma = 0.1$ and different values of a, we compare the values $\Sigma^2(\lambda_0)/\sigma^2$ from (D.2) with the estimated values Σ^2/σ^2 obtained numerically from the truncated system (3.3).

a	$\Sigma^2(\lambda_0)/\sigma^2$ from (D.2)	Estimated Σ^2/σ^2
0	0.5	0.48
0.2	0.57	0.55
0.5	0.75	0.72
0.8	1.12	1.03

roll pattern is stable, as compared to $r_c = 0$ for the deterministic SHE and SHE+P. This type of result was obtained for the stochastic SHE in [39] for the case $a\tau = 0$. The value of Σ^2 (and thus also r_c for $\sigma \neq 0$) increases for values of $a\tau$ closer to unity as shown in Table 1, where the estimated Σ obtained from the truncated amplitude system (3.3) is compared with the analytical approximation $\Sigma^2(\lambda_0)$ given in Appendix D. Similarly, the value $2\varepsilon\rho_0$ compares well with the average amplitude obtained numerically from the truncated system (not shown), with ρ_0 decreasing with increasing $a\tau$. From the stability analysis of (3.10) we also find complex eigenvalues for $1 - a\tau = O(\varepsilon^2)$ or smaller, which play an important role in the spectral dynamics.

3.2. Spectral analysis

While (3.10) describes the long time averaged behavior of the pattern, it does not capture the spectral behavior. Recall from the analysis of (2.10), that for $1 - a\tau = O(\varepsilon)$ or smaller the amplitude of the pattern exhibits oscillations on the S time scale as it evolves toward the steady pattern. This result is also found from a stability analysis of steady states of (3.10), which has the same form as (2.10). The complex eigenvalues of the underlying linearization describe temporal oscillations in the deterministic SHE+P that are damped on a slow time scale, which can be sustained over time through the interaction with noise. This phenomenon is commonly known as coherence resonance, and can be understood by analyzing the amplitude equations corresponding to the sustained oscillations (see for example [37,45] and references therein) or via the power spectrum of the stochastic system [46]. In order to capture the effects of these interactions for the SHE+P, we analyze the power spectra of the critical and non-critical modes to identify the sustained frequency content of the amplitude dynamics.

For a stationary process, the spectral density, defined as the Fourier transform of the correlation function D.1, provides its frequency content. From the spectral representation theorem [47] we have that the spectral density of a stationary process is equivalent to the power spectrum of its trajectory.

We find that

Result 3.3. *The spectral densities are*

$$P_Z(f) = \frac{\sigma^2}{2\pi}|H_Z(if)|^{-2} \tag{3.12a}$$

$$P_Y(f) = \frac{(3\varepsilon^2\rho_0)^2}{\pi}|H_Y(if)|^{-2}(P_Z * P_Z)(f), \tag{3.12b}$$

where $Z(t) = A_0(t)$ and $A_1(T) = 2(\rho_0 + Y(\varepsilon^{-2}T))$. The characteristic functions are $H_Z(q) = q - a(1 - e^{-q\tau}) + \Lambda(2\rho_0)$ with Λ as in (3.9) and $H_Y(q) = q - a(1 - e^{-q\tau}) + 6\varepsilon^2\rho_0^2$.

Over long periods where A_1 remains close to $2\rho_0$, we expect that (3.12) provides a good approximation to the power spectra of Z and Y.

These power spectra give approximations for the spectral densities P_Z and P_Y of Z, Y, which we compare with analytical results. Note that the convolution term $P_Z * P_Z$ in P_Y, (3.12b) appears via the spectral density of the centered process $Z^2 - \Sigma^2$.

Derivation of Result 3.3. We consider the system (3.3), for parameter values where the system remains near one of the stable equilibria, e.g. $(A_1, A_{-1}) = (2\rho_0, 0)$, for long times and $r_2 > 3\Sigma^2(\lambda_0)$. In this parameter range we can approximate the power spectrum of the amplitude processes over the time interval on which they remain close to the steady state. We substitute $A_1(T) = 2(\rho_0 + Y(\varepsilon^{-2}T))$ together with the approximation $A_0(t) = Z(t)$, into (3.3a), and linearize in Y, which is viewed as a small perturbation to ρ_0. Similarly we could write $A_{-1} = 0 + y$ for $y \ll 1$. Since the equation for y indicates that it decays, we neglect it in the rest of the calculations. Then we are left with the SDDE for Y,

$$dY = [-6\varepsilon^2\rho_0^2 Y + a(Y - Y(t-\tau))]dt - 3\varepsilon^2\rho_0 \times (Z^2 - \Sigma^2(\lambda_0))dt \tag{3.13}$$

Note that this equation is coupled with the SDDE (3.8) for Z. Both $Y(t), Z(t)$ are expressed as functions of the fast time t, and we have neglected the term $\varepsilon^2 Y(Z^2 - \Sigma^2)$, which is assumed to be small with respect to the last term in (3.13).

Appendix D summarizes the results of [44] for the stationary solution and spectral density of Z, and derives these quantities for Y from (3.13).

4. Numerical results for the stochastic SHE+P

First we give numerical results for the spectral densities in Result 3.3 and compare with the analytical results of the previous section. Fig. 4 shows the time evolution, distribution and power spectra of the two amplitudes u_1 and u_0, obtained from the projections $u_k = \mathcal{P}_k(u)$ where u is the simulation of the solution of the stochastic SHE+P in the range $a\tau$ near unity. The figure compares these with the behavior as predicted by the asymptotic approximations, and we verify that the statistical properties of the numerical solution of the stochastic SHE+P match the behavior obtained through the asymptotic approximations. The numerically estimated mean for $u_1(t)$ is $0.2151 \approx 2\varepsilon\rho_0 = 0.2149$, and the numerical estimates for the mean and variance of $u_0(t)$ are, respectively, 2.907×10^{-4} and $\hat{\Sigma}^2 = 0.00172 \approx \varepsilon^2\Sigma^2 = 0.00179$. Furthermore, we accept the null hypothesis of the Jarque–Bera test [48] for normality of u_0 (with p-value $= 0.0675$). In the simulation the solution u remains close to the stable pattern, so that the appropriately normalized power spectra have good agreement with the spectral densities (3.12).

As already shown in Fig. 2 for the deterministic system, there is a difference in the underlying behavior of the transient, related to the eigenvalues for the system linearized about the equilibrium corresponding to rolls. In the stochastic system, this difference can be observed in the behavior of the power spectra for $a\tau$ near 1 and $a\tau$ near 0, as illustrated in the behavior of P_Z and P_Y given in (3.12) and compared with simulations of the full stochastic SHE+P in Figs. 4 and 5.

Result 4.1. *For $a\tau$ near 1, the spectral density P_Z is peaked around the frequency corresponding to the imaginary part of the eigenvalues for the linear operator in (3.8). This behavior indicates the phenomenon of coherence resonance* [45]*, where the noise sustains oscillations that are weakly damped. A straightforward computation of the eigenvalues for the linear operator in (3.8) shows that the real part of the eigenvalues are negative and decreasing in magnitude as $a\tau$ approaches unity, yielding noise-sustained oscillations as illustrated for other stochastic differential delay equations in* [37].

It is straightforward to show that this peak in $P_Z(f)$ at nonzero values of frequency is observed only for $a\tau$ closer to 1, corresponding to values of $a > 0$ and $\tau > 0$ such that $P_Z''(0) > 0$. Furthermore, for $a\tau$ near 1 there is a band of $O(\varepsilon)$ frequencies

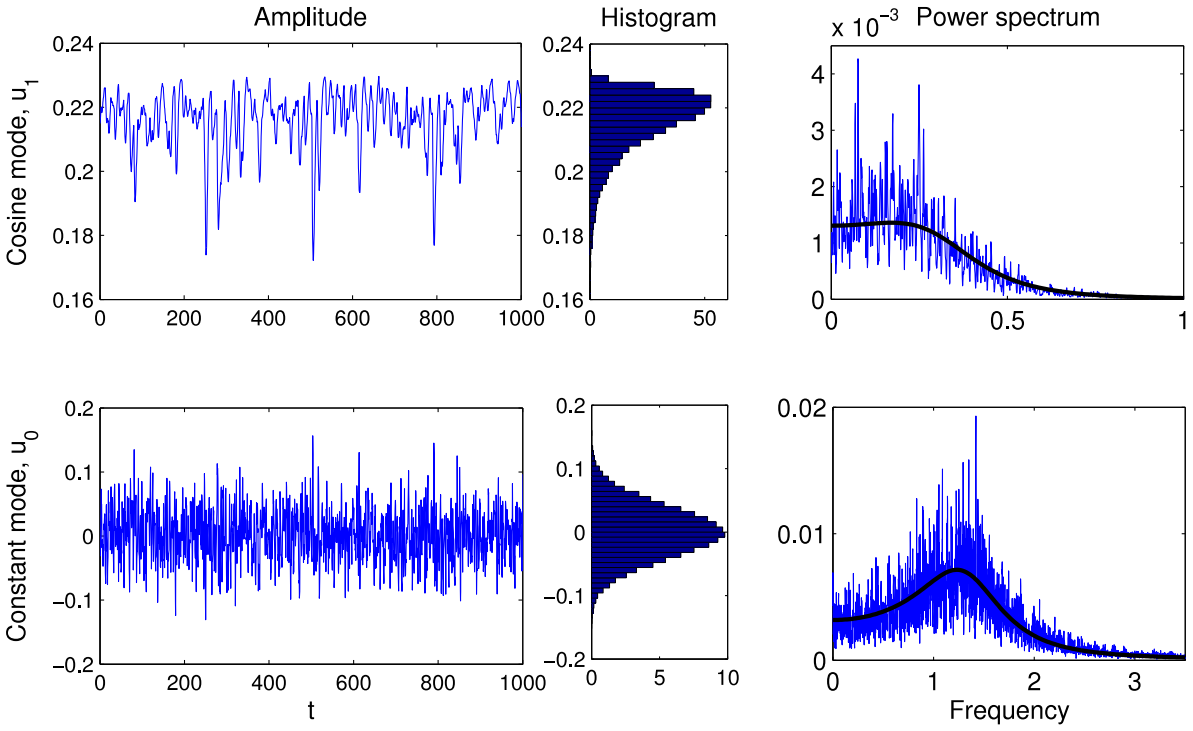

Fig. 4. Results for the numerical solution of the stochastic SHE+P equation. The parameters are $a = 0.8, \tau = 1, r_2 = 1, \varepsilon = 0.2, \sigma = 0.2$, with initial condition $u(t, x) = 2\varepsilon\rho_0 \cos x$ on $-\tau \le t \le 0$ with $\rho_0 = 0.537$, which is near the value for the stable roll pattern with amplitude determined from the average equation as in (3.11). Simulations are run to $t = 20\,000$. LEFT & CENTER: Time evolution and histogram (normalized) of the amplitude of the cosine mode (top) and constant mode (bottom). In general, for $\sigma = O(1)$ the system remains for long times near the equilibrium $(A_1, A_{-1}) = (2\rho_0, 0)$. RIGHT: Power spectrum on the t time scale. The solid lines are the rescaled approximate spectral densities P_Y (top) and P_Z (bottom) given in (3.12). The peak in P_Z corresponds to the root of H_Z.

in P_Y that do not decay exponentially. As shown in the stability analysis of the deterministic amplitude equation based on (2.21), the system linearized about the rolls has eigenvalues with $O(\varepsilon)$ imaginary part for $a\tau$ near 1, corresponding to the complex root of H_Y. Thus the system exhibits oscillations on the S time scale, which are sustained in the stochastic setting through the stochastic forcing from $Z^2 - \sigma^2$. In contrast, for $a\tau$ near 0, the roots of both H_Y and H_Z are real, corresponding to strong damping, no oscillations, and power spectra that decay rapidly from $f = 0$.

Fig. 5 compares the power spectra of A_1, A_0 obtained from the truncated amplitude system (3.3) with the asymptotic approximation for the spectral densities in (3.12). For $a\tau = 0$, the power spectra decay immediately from $f = 0$ with $P_Z \sim 1/f^2$ and $P_{A_1} \sim 1/f^4$. As $a\tau$ is increased toward 1, the sustained frequencies include an $\mathcal{O}(\varepsilon)$ band for the cosine mode, and $\mathcal{O}(1)$ band of frequencies for the constant mode. For higher frequencies, the spectra decay as described for $a\tau$ near zero for both the asymptotic approximation and numerically computed power spectra.

Simulations of the full stochastic SHE+P equation shown in Fig. 6 illustrate how the spectral behavior appears in the spatio-temporal patterns. For $a\tau$ near 1, the temporal random fluctuations of the Ornstein–Uhlenbeck-type process Z do not show any evidence of a preferred frequency, while for $a\tau$ near 1, these fluctuations increase with evidence of the peak in the power spectral densities shown in Figs. 4 and 5. For larger values of the noise and $a\tau$ near 1, there are occasional rapid phase flips corresponding to the pattern shifting between solutions near the locally stable steady states of (3.10) with $(A_1, A_{-1}) = (2\rho_0, 0)$ and symmetrically $(A_{-1}, A_1) = (2\rho_0, 0)$. Larger oscillations from combined delayed feedback and noise drive these transitions between phase shifted roll-type patterns. We do not study them in this paper, but provide some discussion in Section 5.

5. Discussion and future directions

Through a multiple time scale analysis of the Swift–Hohenberg equation with delayed feedback via Pyragas control, we provide several new insights into the dynamics with and without additive noise. The analysis of the onset of patterns shows Turing bifurcations for $0 < a\tau < 1$ at bifurcation parameter values $r = 0$ and Turing–Hopf bifurcations for $a\tau > 1$ at a non-zero and negative value of $r = r_c$. In the deterministic context, for $r = \epsilon^2 r_2$ we derive a Ginzburg–Landau-type equation for the amplitude of the rolls, leading to Eckhaus stability criteria for the rolls. Besides the usual time scales of t and $T = \epsilon^2 t$, there is an intermediate time scale $S = \epsilon t$ observed in the transients for values of $1 - a\tau = O(\epsilon)$ or smaller. In the stochastic context, we derive a system of equations coupling the dynamics of the amplitude of the primary mode on the slow time scale T to the fast dynamics of the zero mode corresponding to the additive noise, described by an Ornstein–Uhlenbeck-type equation with delay. By deriving an averaging approximation for the amplitude of the primary mode, we show how the interaction of noise and delays influences the existence and stability range for the noisy roll-type patterns. Furthermore, approximations for the spectral densities of the primary and zero modes show that the interaction of noise and delay results in sustained oscillations on the intermediate times scale $S = \varepsilon t$, in contrast to the deterministic context where dynamics on the intermediate times scale are transient.

The results of this paper point to a number of areas for future asymptotic analysis. The first of these is the analysis of Turing–Hopf bifurcations for $a\tau > 1$, which are not observed for the SHE without delay. The analysis provided in this paper should be straightforward to apply in the Turing–Hopf case, for deriving spatial–temporal amplitude equations for $a\tau > 1$ and for studying different stability criteria.

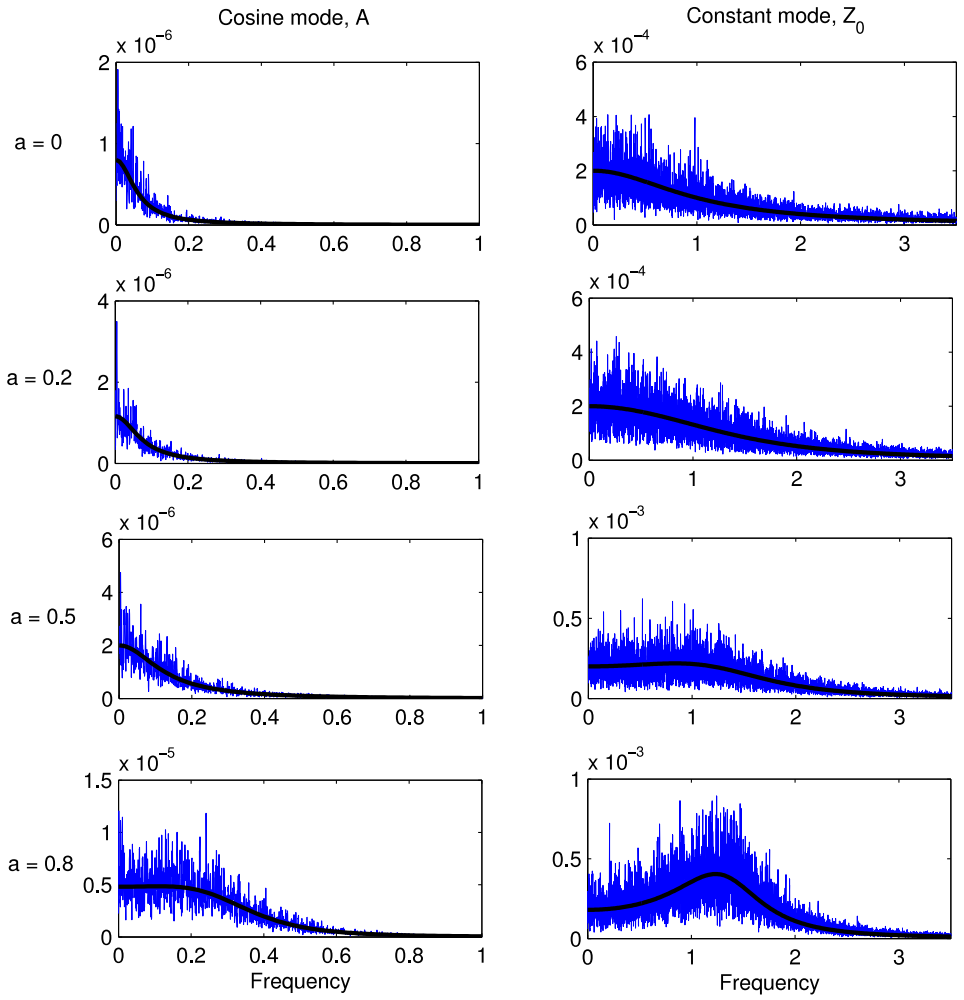

Fig. 5. Power spectra for the amplitudes of the cosine and constant modes A_1 and A_0, for different values of a. The solid black lines are the rescaled spectral densities in (3.12). The parameters are those used in Table 1. Simulations are run for times up to $t \le t_{max} = 50000$, during which the amplitudes remained close to the steady value, so that the assumptions are satisfied for obtaining the approximations (3.12).

As motivated by the bottom panel in Fig. 6, for larger values of the noise there is an additional phenomenon driven by the interaction of delay and noise that is not observed in previous models. The figure shows the possibility for regular phase flips, corresponding to the transitions between the stable equilibria of (3.3) for the primary mode, $(A_1, A_{-1}) = (2\rho_0, 0)$ and $(A_{-1}, A_1) = (2\rho_0, 0)$. These phase flips can be studied via the full nonlinear coupled system (3.3) for the amplitudes of the dominant and noisy modes, which can be expressed as a gradient system with delay and degenerate noise,

$$d\mathbf{X}(t) = -\nabla V(\mathbf{X}(t)) + a(\mathbf{X}(t) - \mathbf{X}(t-\tau)) + \begin{pmatrix} \mathbf{0} \\ \sigma\, dW(t) \end{pmatrix}.$$

Here V is a quartic potential, with the phase flips corresponding to phase transitions between the attracting wells of V. These occur relatively frequently for larger values of σ, where the linearization used for the spectral analysis in Section 3 is no longer valid. Transitions of this type have been studied in related one dimensional time-delayed bi-stable stochastic systems [49–51]. However, it appears that these types of transitions have not been studied in coupled stochastic systems with delayed feedback. Preliminary explorations suggest that the geometry of the wells near the attracting equilibria, together with the interaction of noise and delay, are all important features in the prevalence of transitions between the wells.

Acknowledgments

This work was partially supported by a grant from the Simons Foundation for work carried out in part at the Isaac Newton Institute and by a Natural Sciences and Engineering Research Council (NSERC) Discovery Grant (22R23106).

Appendix A. The transcendental equation and its solution branches

We show some fundamental results for the transcendental equation

$$\omega = \mu(k, r) + a(1 - e^{-\omega\tau}) \tag{A.1}$$

for parameters $a, \tau > 0$, and $\mu = \mu(k, r)$ as defined in Section 2.1. It is well-known that there are infinitely many solutions for ω given by

$$\omega_m(k, r) = \mu(k, r) + a + \frac{1}{\tau} W_m(-a\tau e^{-\tau(a+\mu)}),$$
$$\text{for } m \in \mathbb{Z}. \tag{A.2}$$

Here, $W_m(z)$ denotes the branches of the Lambert functions, which are defined as the multi-valued inverse of the complex function $w \mapsto we^w$ [52]. Accordingly, we shall call ω_m the branches of ω, and call ω_0 the *principle branch* of ω corresponding to the principle

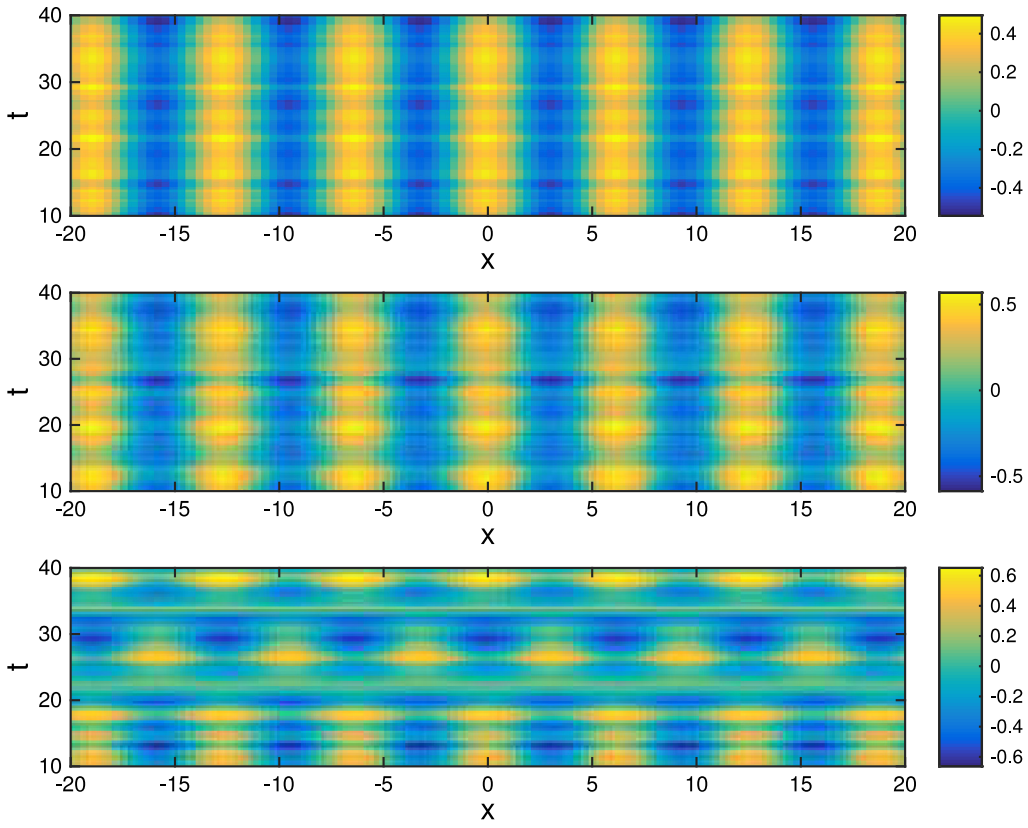

Fig. 6. Results of the numerical simulations of the solution u of the full stochastic SHE+P, with initial condition $u(x,0) = 2\varepsilon(\rho_0+\rho)\cos x$ ($K=0$), ρ_0 given in (2.18), and $\rho = 0.1$. For all figures, $\tau = 1$, $\varepsilon = 0.2$, $r_2 = 3$. The solution u is plotted as function of x (horizontal axis) and t (vertical axis) where the colors represent large (yellow) or smaller (blue) values of u. Top: Random fluctuations in time in the amplitude of the roll pattern, as driven by the OU-type process Z, with $a\tau = 0.2$, $\sigma = 0.4$; Middle: For $a\tau = 0.9$ and $\sigma = 0.4$, coherence resonance drives larger temporal fluctuations in the roll pattern, with evidence of the peak in the power spectra as shown in Fig. 5 for larger $a\tau$. Bottom: For $a\tau = 0.9$, $\sigma = 0.7$, increased magnitude of oscillations can lead to occasional rapid phase flips, corresponding to transitions between solutions near the steady states, $(A_1, A_{-1}) = (2\rho_0, 0)$ and $(A_{-1}, A_1) = (2\rho_0, 0)$. (For interpretation of the references to color in this figure legend, the reader is referred to the web version of this article.)

branch W_0 of the Lambert function. For these Lambert functions several properties are known.

Properties of the Lambert functions W_m

(i) $W_0(z)$ takes real arguments $z \in [-1/e, \infty)$ onto real values and real arguments $z \in (-\infty, -1/e)$ onto complex values.
(ii) only $W_m(z)$ for $m = 0, -1$ may take real values whereas $W_m(z)$, $m \neq 0, -1$ are complex.

Since we are interested in the change in sign of the real part of the leading eigenvalue, as well as its corresponding imaginary part, we summarize relevant properties of the branches ω_m that follow from the above properties of the Lambert functions.

Properties of the branches of ω_m

(i) $Re(\omega_0) \geq Re(\omega_{-1})$, and $Re(\omega_0) > Re(\omega_m)$ for all $m \neq 0, -1$, so that ω_0 is the leading eigenvalue of Eq. (A.1).
(ii) Let

$$\mu^* := (\ln(a\tau) + 1 - a\tau)/\tau.$$

(that is, $-a\tau e^{-(a+\mu^*)\tau} = -1/e$.) For the branches ω_0 and ω_{-1}, it holds that

(a) if $\mu > \mu^*$, then $\omega_{0,-1}$ are both real, and $\omega_{-1} < \ln(a\tau)/\tau < \omega_0$.
(b) if $\mu = \mu^*$, then $\omega_0 = \omega_{-1} = \ln(a\tau)/\tau$.
(c) if $\mu < \mu^*$, then $\overline{\omega_0} = \omega_{-1}$, and $Re(\omega_0) < \ln(a\tau)/\tau$, and $Im(\omega_0) \in (0, \frac{\pi}{\tau})$.

(iii) The function $\mu \mapsto Re(\omega_0)$ is continuous and strictly increasing in μ. It is also differentiable for $\mu \neq \mu^*$.

A.1. Proof of Result 2.1

Since $Re(\omega_0)$ is increasing with μ by property (iii), it first changes sign at the maximum of $\mu = \mu(k, r)$ at $k = k_c = \pm 1$, where $\mu(k_c, r) = r > \mu^*$. We look for $r = r_c$ and $\nu = \nu_c$ where $Re(\omega_0)$ changes sign, that is, $\omega_0(k_c, r_c) = i\nu_c$, for some $\nu_c \in [0, \pi/\tau)$. Substituting $\omega = i\nu$ into (A.1) and separating into real and imaginary parts yields

$$r + a = a\cos(\nu\tau) \tag{A.3a}$$

$$\nu = a\sin(\nu\tau). \tag{A.3b}$$

When $a\tau < 1$, $\nu = r = 0$ is the only solution of (A.3) and $\ln(a\tau) < 0$, which corresponds to case (a) under property (ii) above. Then the critical values of r and ν corresponds to $\omega_0(k_c, 0)$ where

$$\omega_{-1}(k_c, 0) < \frac{1}{\tau}\ln(a\tau) < \omega_0(k_c, 0) = 0.$$

so that $r_c = 0$, $\nu_c = 0$.

When $a\tau > 1$, there are at least two real solutions of (A.3b), $\nu = 0$ and some $\nu \in (0, \pi/\tau)$, which is straightforward to show graphically. From property (ii) only the branches ω_0, ω_{-1} can take real values, and $\ln(a\tau) > 0$ when $a\tau > 1$. Furthermore, property (ii) implies that

$$0 = Re(\omega_{-1}(k_c, 0)) < \frac{1}{\tau}\ln(a\tau) < Re(\omega_0(k_c, 0)),$$

so that $\nu = 0$ corresponds to ω_{-1} and $\omega_0 > 0$ for $r = 0$. Then the critical value of r is $r_c = a(\cos(\nu_c\tau) - 1) < 0$.

Appendix B. Asymptotic behavior of ω_0 for $\mu = O(\epsilon^2)$

We consider the asymptotic behavior of the primary branch ω_0 of (A.2), with $\mu = \mu(1+\varepsilon K, \varepsilon^2 r_2) = \epsilon^2(r_2 - 4K^2 + \mathcal{O}(\varepsilon))$ as in Section 2.1. There are two cases of interest, motivated by the behavior of $W_0(-a\tau e^{-\tau(a+\mu)})$ in (A.2). We consider the argument of W_0, using that $1 \gg \mu = O(\epsilon^2)$,

$$\begin{aligned} &W_0(-a\tau e^{-a\tau}(1-\mu\tau+(\mu\tau)^2/2+\cdots)) \\ &= W_0(-(1-\delta)e^{-(1-\delta)}(1-\mu\tau+(\mu\tau)^2/2+\cdots,)) \end{aligned} \tag{B.1}$$

where $\delta = (1-a\tau)$. For $\delta = \mathcal{O}(1)$ and $\varepsilon \ll 1$ (so that $\mu \ll 1$) we can use a Taylor expansion for W_0 around $a\tau e^{-a\tau}$. In contrast, for $\delta \ll 1$ as well as $\varepsilon \ll 1$ (so still $\mu \ll 1$), the argument of W_0 approaches the singularity of $W_0(z)$ at the branch point $z = -1/e$, so we must use a series expansion about this point. Next, we analyze these cases separately.

Case (i) $\delta = \mathcal{O}(1)$ and $\varepsilon \ll 1$.

We apply the Taylor series expansion of $W_0(z)$ in (B.1) around the value $z = -a\tau e^{-a\tau}$

$$W(-a\tau e^{-a\tau}(1-\mu\tau+\mathcal{O}(\mu^2))) = -a\tau + \frac{a\tau}{1-a\tau}\mu\tau + \mathcal{O}(\mu^2),$$

where we used that $W(-a\tau e^{-a\tau}) = -a\tau$ and $W'(z) = \frac{W(z)}{z(1+W(z))}$. Substituting in (A.2) yields

$$\omega_0 = \frac{\mu}{1-a\tau} + \mathcal{O}(\mu^2) = \frac{\mu}{\delta} + \mathcal{O}(\mu^2). \tag{B.2a}$$

Note that δ appears in the denominator of (B.2), so this approximation is not valid in the case when $\delta \ll 1$.

Case (ii) $\delta \ll 1$ and $\varepsilon \ll 1$.

We apply the series expansion of $W_0(z)$ about the branch point $z = -\frac{1}{e}$ [52], which is given by

$$W_0(-1/e+y) = -1 + \sqrt{2ey} - \frac{2ey}{3} + \mathcal{O}(y^{\frac{3}{2}}),$$

for $y \ll 1$. Then, we get

$$\begin{aligned} &W_0\left(-(1-\delta)e^{-(1-\delta)}(1-\mu\tau+O(\mu^2))\right) \\ &\quad = W_0\left(-e^{-1}+e^{-1}\left(\mu\tau+\frac{1}{2}\delta^2+\mathcal{O}(\mu^2,\delta^3)\right)\right) \\ &\quad = -1+\sqrt{2\mu\tau+\delta^2+\mathcal{O}(\mu^2,\delta^3)} - \frac{1}{3}\left(2\mu\tau+\delta^2+\mathcal{O}(\mu^2,\delta^3)\right) \end{aligned}$$

so that from (A.2), the leading order terms are

$$\omega_0 = \frac{1}{3}\mu - \frac{\delta}{\tau} + \frac{1}{\tau}\sqrt{2\mu\tau+\delta^2+\mathcal{O}(\mu^2,\delta^3)}. \tag{B.2b}$$

The results of Sections 2.1 and 2.3 focus on the magnitude of $\delta = (1-a\tau)$ relative to $\epsilon \ll 1$, specifically $(1-a\tau) = O(1)$ and $(1-a\tau) = O(\epsilon)$ or smaller. Writing $\mu = \epsilon^2\tilde{\mu}$ and combining the results in (B.2), we obtain expressions for the leading order behavior of ω_0 for the different relationships between $(1-a\tau)$ and ε,

$$\omega_0 = \begin{cases} \varepsilon\sqrt{2\tilde{\mu}/\tau} + \varepsilon^{1+(\kappa\wedge 1)}H, & \text{if } 1-a\tau = C\varepsilon^{1+\kappa} \text{ with } \kappa > 0 \\ \varepsilon\left(-C+\sqrt{2\tau\tilde{\mu}+C^2}\right)/\tau, & \text{if } 1-a\tau = C\varepsilon \\ \varepsilon^{1+\kappa}\tilde{\mu}/C, & \text{if } 1-a\tau = C\varepsilon^{1-\kappa} \text{ with } 0<\kappa\le 1 \end{cases} \tag{B.3}$$

where $H = \frac{\tilde{\mu}}{3}\mathbf{1}_{\kappa\ge 1} - \frac{C}{\tau}\mathbf{1}_{\kappa\le 1}$ and $\wedge$ indicates the minimum.

A similar approach is used to obtain the results for Ω in Section 2.3 by replacing μ and ω in (B.3) with $\varepsilon^2 h_\pm$ and $\epsilon^2\Omega$, respectively. In Section 2.3, $\tilde{\mu} = h_\pm$ may be negative, resulting in complex values of Ω in both the first case of (B.3) and in the second case for $(1-a\tau)^2 < |2\tau\epsilon^2 h_\pm|$,

Appendix C. Solvability condition for SHE with delay

Let $\mathcal{S}$ be the linearized Swift–Hohenberg operator with Pyragas control defined in (2.9). Denote its formal adjoint by

$$\mathcal{S}^*u = -u_t + (1+\partial_x^2)^2 u - a(u - u(t+\tau))$$

and let $\mathcal{N}(\mathcal{S}^*)$ be the null space of $\mathcal{S}^*$. We derive a necessary condition for the IVP

$$\mathcal{S}u = g(t,x) \qquad \text{on } (t,x) \in [0,\infty)\times\mathbb{R} \tag{C.1a}$$

$$u(t,x) = 0 \qquad \text{on } -\tau \le t \le 0 \tag{C.1b}$$

to have a smooth sublinearly growing solution.

Lemma C.1. *If the IVP (C.1) has a solution $u(t) \in W^{3,1}(\mathbb{R})$ that grows sublinearly in time, i.e., $\lim_{t\to\infty}\frac{|u(t)|_{L^1}}{t} = 0$, then*

$$\lim_{T\to\infty}\frac{1}{T}\int_0^T\int_{\mathbb{R}} wg\,dxdt = 0 \tag{C.2}$$

for all $w \in \mathcal{N}(\mathcal{S}^*)$ such that $\sup_{(t,x)\in[0,\infty)\times\mathbb{R}}|w(t,x)| < \infty$.

The proof follows from a standard application of integration-by-parts[1] and the adjoint of the Pyragas term. Condition (C.2), that g is orthogonal to the space of bounded functions in $\mathcal{N}(\mathcal{S}^*)$, is the solvability condition for (C.1). The next result that the only bounded solutions in $\mathcal{N}(\mathcal{S}^*)$ are the resonant modes of $\mathcal{S}$ follows since the dispersion relation for $\mathcal{S}^*$ is the same as (2.3), apart from replacing ω by $-\omega$, .

Lemma C.2. *The solution $e^{i\tilde{k}x+\tilde{\omega}t}$ is a uniformly bounded function in $\mathcal{N}(\mathcal{S}^*)$ if and only if $\tilde{k} = k_c$ and $\tilde{\omega} = i\nu_c$ are the critical parameters in Result 2.1.*

Appendix D. Stationarity and spectral density for linear stochastic DDEs

We show the stationary solutions and spectral density using the linearized SDDEs (3.8) and (3.13) for the random variables Z and Y, respectively. We use the following definitions for (mean zero) stationary processes:

Definition D.1. A complex-valued stochastic process X_t on $(-\infty,\infty)$, is *(second order) stationary* if, for all t, s, $\mathbb{E}|X_t|^2 < \infty$, $\mathbb{E}X_t$ is constant, and $\mathbb{E}X_tX_{t+s}$ depends only on s. The *correlation function* of X_t is $K(s) := \mathbb{E}[X_tX_{t+s}]$. The *spectral density* $P(f)$ of X_t corresponding to the correlation function $K(s)$ is the Fourier transform of K; that is, $K(s) = \int_{\mathbb{R}} e^{ifs}P(f)df$.

The stationarity and spectral density for (3.8) are given in [44]. The stationary solution of (3.8) is

$$Z(t) = \int_{-\infty}^{t} z(t-s)\sigma\,dB(s), \quad t \ge -\tau,$$

where z is the fundamental solution of

$$\begin{aligned} &\dot{z}(t) = -\Lambda z(t) + a(z(t) - z(t-\tau)) \\ &z(t) = \mathbf{1}_{\{0\}}(t), \qquad \text{for } -\tau < t \le 0, \end{aligned} \tag{D.1}$$

with $\mathbf{1}$ the indicator function. The stationary distribution of Z is a centered Gaussian process, $Z(t) \sim N(0, \Sigma^2(\Lambda))$, with variance

[1] More generally, [53] showed a Fredholm Alternative for functional differential equations using Green's functions.

$$\Sigma^2(\Lambda) = \begin{cases} \dfrac{-a\sinh(l\tau) - l}{2l(a - \Lambda - a\cosh(l\tau))}\sigma^2, & \text{if } 2a < \Lambda \\ \dfrac{a\tau + 1}{4a}\sigma^2, & \text{if } 2a = \Lambda \\ \dfrac{-a\sin(l\tau) - l}{2l(a - \Lambda - a\cos(l\tau))}\sigma^2, & \text{if } 2a > \Lambda \end{cases}, \qquad \text{(D.2)}$$

where $l = |\Lambda^2 - 2a\Lambda|^{1/2}$. The covariance function of Z is

$$K_Z(s) = \int_0^\infty z(t+s)z(t)\sigma^2 dt, \qquad t \geq 0$$

and $K_Z(s) = K_Z(-s)$. Taking the Fourier transform of K_Z, the spectral density is

$$P_Z(f) = \frac{\sigma^2}{2\pi}|H_Z(if)|^{-2} \qquad \text{(D.3)}$$

where $H_Z(q) = q + \Lambda - a(1 - e^{-q\tau})$ is the characteristic function for (D.1).

The approximation $\Sigma^2(\Lambda) \sim \Sigma^2(\lambda_0)$ is used in Section 3 to derive Eq. (3.13) for Y, which can be solved to get

$$Y(t) = \int_{-\infty}^t y(t-s)\cdot 3\varepsilon^2\rho_0(Z^2(s) - \Sigma^2)ds,$$

where y is the fundamental solution solving (D.1) with $6\epsilon^2\rho_0^2$ in place of Λ. The stochastic forcing is not white noise, but rather $\xi(t) := Z^2(t) - \Sigma^2$. Clearly, $\mathbb{E}\xi(t) = 0$, and we show that ξ is a centered second-order stationary process. As noted in [44], Z satisfies a stronger form of stationarity where the finite dimensional distributions $(Z(t_1), \ldots, Z(t_n))$ are jointly multivariate normal distributed, so that

$$(Z(t), Z(t+s)) \sim N(0, \Gamma(s)), \qquad \text{where } \Gamma(s) = \begin{pmatrix} K_Z(0) & K_Z(s) \\ K_Z(s) & K_Z(0) \end{pmatrix}.$$

Then $\mathbb{E}[Z^2(t)Z^2(t+s)]$ depends only on s but not t, and the covariance function of ξ can be computed (using the moment generating function)

$$\begin{aligned} K_\xi(s) &:= \mathbb{E}[\xi(t)\xi(t+s)] = \mathbb{E}[Z^2(t)Z^2(t+s)] - \Sigma^4 \\ &= \left(2K_Z^2(s) + K_Z^2(0)\right) - \Sigma^4 = 2K_Z^2(s). \end{aligned}$$

Hence, ξ is a centered second-order stationary process. Taking the Fourier transform of K_ξ yields the spectral density of ξ, $P_\xi(f) = 2(P_Z * P_Z)(f)$, where $*$ denotes convolution.

The covariance function of Y can be obtained through direct computation using K_ξ

$$\begin{aligned} K_Y(s) &= \mathbb{E}[Y(t)Y(t+s)] \\ &= (3\varepsilon^2\rho_0)^2\mathbb{E}\left[\int_{-\infty}^t y(t-r)\xi(r)dr \right. \\ &\quad \left. \times \int_{-\infty}^{t+s} y(t+s-r')\xi(r')dr'\right] \\ &= (3\varepsilon^2\rho_0)^2\int_0^\infty\int_0^\infty y(t)y(r)K_\xi(|s-r+t|)drdt, \end{aligned}$$

implying that Y is a centered second-order stationary process. Taking the Fourier transform of K_Y yields the spectral density for Y,

$$\begin{aligned} P_Y(f) &= \frac{(3\varepsilon^2\rho_0)^2}{2\pi}|H_Y(if)|^{-2}\cdot P_\xi(f) \\ &= \frac{(3\varepsilon^2\rho_0)^2}{2\pi}|H_Y(if)|^{-2}\cdot 2(P_Z * P_Z)(f), \end{aligned}$$

where $H_Y(q) = q + 6\epsilon^2\rho_0^2 - a(1 - e^{-q\tau})$ is the corresponding characteristic function of the linear operator in (3.13).

References

[1] M.C. Cross, P.C. Hohenberg, Pattern formation outside of equilibrium, Rev. Modern Phys. 65 (1993) 851–1112.
[2] M. Cross, H. Greenside, Pattern Formation and Dynamics in Nonequilibrium Systems, Cambridge University Press, Cambridge, UK, 2009.
[3] R.B. Hoyle, Pattern Formation: An Introduction To Methods, Cambridge University Press, Cambridge, UK, 2006.
[4] L.M. Pismen, Patterns and Interfaces in Dissipative Dynamics, in: Springer Series in Synergetics, Springer, Berlin, 2006.
[5] A. Kraft, S.V. Gurevich, Time-delayed feedback control of spatio-temporal self-organized patterns, in: E. Schöll, S.H.L. Klapp, P. Hövel (Eds.), Dissipative Systems, in: Control of Self-Organizing Nonlinear Systems Series Understanding Complex Systems, 2016, pp. 413–430.
[6] M. Tlidi, A. Sonnino, G. Sonnino, Delayed feedback induces motion of localized spots in reaction–diffusion systems, Phys. Rev. E 87 (2013) 042918.
[7] J. Garcia-Ojalvo, J.M. Sancho, Noise in Spatially Extended Systems, Springer-Verlag, New York, 1999.
[8] H. Song, D. Chen D. W. Li, Y. Qu, Graph-theoretic approach to exponential synchronization of stochastic reaction–diffusion Cohen-Grossberg neural networks with time-varying delays, Neurocomputing 177 (2016) 179–187.
[9] T.E. Woolley, R.E. Baker, E.A. Gaffney, P.K. Maini, S. Seirin-Lee, Effects of intrinsic stochasticity on delayed reaction–diffusion patterning systems, Phys. Rev. E 85 (2012) 051914.
[10] Z.P. Kilpatrick, Delay stabilizes stochastic motion of bumps in layered neural fields, Physica D 295–296 (2015) 30–45.
[11] S. Sen, P. Ghosh, D.S. Ray, Reaction–diffusion systems with stochastic time delay in kinetics, Phys. Rev. E 81 (2010) 056207.
[12] J. Swift, P.C. Hohenberg, Hydrodynamic fluctuations at the convective instability, Phys. Rev. A 15 (1977) 319–328.
[13] K. Pyragas, Continuous control of chaos by self-controlling feedback, Phys. Lett. A 170 (1992) 421–428.
[14] M. Tlidi, A.G. Vladimirov, D. Pieroux, D. Turaev, Spontaneous motion of cavity solitons induced by a delayed feedback, Phys. Rev. Lett. 103 (2009) 103904.
[15] L.A. Peletier, V. Rottschäfer, Pattern selection of solutions of the Swift-Hohenberg equation, Physica D 194 (2004) 95–126.
[16] L.A. Peletier, W.C. Troy, Spatial Patterns: Higher Order Models in Physics and Mechanics, Birkhäuser, Boston, 2001.
[17] D. Avitabile, D.J.B Lloyd, J. Burke, E. Knobloch, B. Sandstede, To snake or not to snake in the planar Swift-Hohenberg equation, SIAM J. Appl. Dyn. Syst. 9 (2010) 704–733.
[18] C.J. Budd, R.A. Kuske, Localised periodic patterns for the non-symmetric generalized Swift-Hohenberg equation, Physica D 208 (2005) 73–95.
[19] J. Burke, E. Knobloch, Localized states in the generalized Swift-Hohenberg equation, Phys. Rev. E 73 (2006) 056211.
[20] S.J. Chapman, G. Kozyreff, Exponential asymptotics of localised patterns and snaking bifurcation diagrams, Physica D 238 (2009) 319–354.
[21] J.H.P. Dawes, The emergence of a coherent structure for coherent structures: localized states in nonlinear systems, Phil. Trans. R. Soc. A 368 (2010) 3519–3534.
[22] M. Tlidi, A.G. Vladimirov, D. Turaev, G. Kozyreff, D. Pieroux, T. Erneux, Spontaneous motion of localized structures and localized patterns induced by delayed feedback, Eur. Phys. J. D 59 (2010) 59–65.
[23] M. Tlidi, E. Averlant, A. Vladimirov, K. Panajotov, Delay feedback induces a spontaneous motion of two-dimensional cavity solitons in driven semiconductor microcavities, Phys. Rev. A 86 (2012) 033822.
[24] K. Panajotov, M. Tlidi, Spontaneous motion of cavity solitons in vertical-cavity lasers subject to optical injection and to delayed feedback, Eur. Phys. J. D 59 (2010) 67–72.
[25] K. Montgomery, M. Silber, Feedback control of traveling wave solutions of the complex Ginzburg Landau equation, Nonlinearity 17 (2004) 2225–2248.
[26] C.M. Postlethwaite, M. Silber, Spatial and temporal feedback control of traveling wave solutions of the two-dimensional complex Ginzburg-Landau equation, Physica D 236 (2007) 65–74.
[27] S.V. Gurevich, R. Friedrich, Instabilities of localized structures in dissipative systems with delayed feedback, Phys. Rev. Lett. 110 (2013) 014101.
[28] D. Blömker, Amplitude Equations for Stochastic Partial Differential Equations, RWTH Aachen, 2005, (Habilitationsschrift).
[29] D. Blömker, M. Hairer, G.A. Pavliotis, Modulation equations: stochastic bifurcation in large domains, Comm. Math. Phys. 258 (2005) 479–512.
[30] D. Blömker, M. Hairer, G.A. Pavliotis, Stochastic Swift-Hohenberg equation near a change of stability, Proceedings of Equadiff-11 (2005) 27–37.
[31] D. Blömker, W.W. Mohammed, Amplitude equations for SPDEs with cubic nonlinearities. Stochastics, 85, 181–215.
[32] K. Klepel, D. Blömker, W.W. Mohammed, Amplitude equation for the generalized Swift-Hohenberg equation with noise, Z. Angew. Math. Phys. 65 (2014) 1107–1126.

[33] W.W. Mohammed, D. Blömker, K. Klepel, Modulation equation for stochastic Swift-Hohenberg equation, SIAM J. Math. Anal. 45 (2013) 14–30.
[34] K. Staliunas, Spatial and temporal spectra of noise driven stripe patterns, Phys. Rev. E 64 (2001) 066129.
[35] J. Viñals, E. Hernández-García, M. San Miguel, R. Toral, Numerical study of the dynamical aspects of pattern selection in the stochastic Swift-Hohenberg equation in one dimension, Phys. Rev. A 44 (1991) 1123.
[36] M. Pradas, G.A. Pavliotis, S. Kalliadasis, D.T. Papageorgiou, D. Tseluiko, Additive noise effects in active nonlinear spatially extended systems, Euro. J. of Appl. Math 23 (2012) 563–591.
[37] M.M. Kłosek, R. Kuske, Multi-scale analysis for stochastic differential delay equations, SIAM Multisc. Model. Simul. (2005) 706–729.
[38] G.A. Pavliotis, A. Stuart, Multiscale Methods: Averaging and Homogenization, Springer, 2008.
[39] A. Hutt, A. Longtin, L. Schimansky-Geier, Additive global noise delays turing bifurcations, Phys. Rev. Lett. 98 (2007) 230601.
[40] L.N. Trefethen, Spectral Methods in MATLAB, in: Software, Environments, and Tools, Society for Industrial and Applied Mathematics (SIAM), Philadelphia, PA, 2000. http://dx.doi.org/10.1137/1.9780898719598.
[41] E. Buckwar, R. Kuske, S. Mohammed, T. Shardlow, Weak convergence of the Euler Scheme for stochastic differential delay equations, LMS J. Comput. Math. 11 (2005) 60–99.
[42] P. Manneville, Dissipative Structures and Weak Turbulence, in: Perspectives in Physics, Academic Press, 1990.
[43] W. Eckhaus, Studies in Nonlinear Stability Theory, in: Springer Tracts in Natural Philosophy, vol. 6, Springer, 1965.
[44] U. Küchler, B. Mensch, Langevin's stochastic differential equation extended by a time-delayed term, Stoch. Rep. 40 (1992) 23–42 1992.
[45] P.H. Baxendale, P.E. Greenwwood, Sustained oscillations for density dependent Markov processes, J. Math. Biol. 63 (2011) 433.
[46] A.J. McKane, T.J. Newman, Predator-Prey cycles from resonant amplification of demographic stochasticity, Phys. Rev. Lett. 94 (2005) 218102.
[47] D.B. Percival, A.T. Walden, Spectral Analysis for Physical Applications, Cambridge University Press, Cambridge, 1993.
[48] C.M. Jarque, A.K. Bera, A test for normality of observations and regression residuals, Internat. Statist. Rev. 55 (1987) 163–172 (implemented in the jbtest function in Matlab).
[49] M. Fischer, P. Imkeller, A two state model for noise-induced resonance in bistable systems with delay, Stoch. Dyn. 5 (2) (2005) 247–270 Special Issue on Stochastic Dynamics with Delay and Memory.
[50] D. Huber, L.S. Tsimring, Dynamics of an ensemble of noisy bistable elements with global time delayed coupling, Phys. Rev. Lett. 91 (2003) 260601.
[51] L.S. Tsimring, A. Pikovsky, Noise-induced dynamics in bistable systems with delay, Phys. Rev. Lett. 87 (2001) 250602.
[52] R.M. Corless, G.H. Gonnet, D.E.G Hare, D.J. Jeffrey, D.E. Knuth, On the Lambert W function, Adv. Comput. Math. 5 (1996) 329–359.
[53] J. Mallet-Paret, The Fredholm alternative for functional-differential equations of mixed type, J. Dynam. Differential Equations 11 (1999) 1–47.